

ABSTRACT

KOHLER, LAUREN ASHLEY. Bayesian Calibration and Machine Learning-based Validation of Distributed Fiber Optic Sensors for Advanced Temperature Sensing in Nuclear Reactors. (Under the direction of Dr. Xu Wu).

The accurate and high-resolution measurement of temperature fields in liquid metal-cooled reactors is crucial for reactor safety, performance monitoring, and predictive maintenance. Traditional thermocouple arrays provide reliable temperature data but are limited by sparse spatial resolution and multiple penetrations through pressure boundaries, leading to increased maintenance costs and structural vulnerabilities. Distributed fiber optic sensors (DFOS) offer an alternative, enabling continuous, high-resolution temperature sensing with minimal vessel penetrations. However, DFOS readings require precise calibration to ensure reliability in extreme environments.

This thesis presents a novel methodology for the calibration and validation of DFOS using Bayesian inference and machine learning techniques. The study employs the Delayed Rejection Adaptive Metropolis (DRAM) algorithm to explore calibration parameters and quantify uncertainty in DFOS temperature readings. Sensitivity analysis, incorporating Pearson and Spearman correlation coefficients, the Morris method, and Sobol' indices, is applied to assess the impact of calibration parameters on the model output. Furthermore, a Long Short-Term Memory (LSTM) autoencoder is utilized to reconstruct temperature fields from sparse thermocouple measurements, providing a robust validation framework for DFOS readings.

The methodology is demonstrated using experimental data from a water flow loop and the Thermal Hydraulic Experimental Test Article (THETA) at Argonne National Laboratory, both equipped with co-located thermocouples and DFOS. Results indicate a strong correlation between thermocouple and DFOS measurements, with Bayesian calibration significantly improving the accuracy of temperature reconstructions. The findings support the feasibility of reducing reliance on thermocouples while maintaining precise temperature monitoring in advanced reactor systems.

LIST OF PUBLICATIONS

1. **L. Kohler**, M. Weathered, D. Lisowski, X. Wu, A. Heifetz. "Bayesian Calibration and Sensitivity Analysis of Fiber Optic Distributed Temperature Sensing in Water," *Submitted to Nuclear Science and Engineering*.
2. **L. Kohler**, M. Weathered, A. Heifetz. "VOCAL: Validation, Optical Calibration and Learning Interactive Graphical Interface for Distributed Temperature Sensing in Advanced Reactors," Transactions of Advances in Thermal Hydraulic Conference. Orlando, Florida, USA. November 17 - 21, 2024.
3. **L. Kohler**, N. Etter, N. Ritchie, M. Diaconeasa. "Event Sequence Quantification and Consequence Development of the Full Scope Dynamic Probabilistic Risk Assessment for PULSTAR Research Reactor," Transactions of American Nuclear Society. Orlando, Florida, USA. November 17 - 21, 2024.
4. **L. Kohler**, D. Lisowski, A. Heifetz. "Global Sensitivity Analysis of Distributed Fiber Optic Temperature Measurements in a Thermal Hydraulic System," Transactions of 2024 International Congress on Advances in Nuclear Power Plants. Las Vegas, Nevada, USA. June 16 - 19, 2024.
5. A. Akins, A. Furlong, **L. Kohler**, J. Clifford, C. Brady, F. Alsafadi, X. Wu. "ARTISANS—Artificial Intelligence for Simulation of Advanced Nuclear Systems for Nuclear Fission Technology," Nuclear Engineering and Design, vol. 423, p. 113170, Jul. 2024.
6. **L. Kohler**, X. Wu, A. Heifetz, "Bayesian Inference and Inverse Uncertainty Quantification of Fiber Optic Distributed Temperature Sensing in a Thermal Mixing Tee" submitted for Proceedings of the ANS Best Estimate Plus Uncertainty International Conference (BEPU-2024). Lucca, Tuscany Italy, May 19 – 24, 2024.
7. **L. Kohler**, J. Clifford, E. Kautz, X. Wu. "ML-Spec: Benchmark Results of Machine Learning-Based Spectra Predictions of Time-Dependent Lithium Emission Spectroscopy Imaging." Submitted for Proceedings of ANS, Pennsylvania, USA, April 4 – 6, 2024.
8. **L. Kohler**, N. Etter, N. Ritchie, M. Diaconeasa. "Enhancing Probabilistic Risk Assessment for the PULSTAR Research Reactor with Advanced Fault Tree and Initiating Event Analysis Techniques." Transactions of American Nuclear Society. University Park, Pennsylvania, USA, April 4 – 6, 2024.

9. **L. Kohler**, M. Weathered, A. Heifetz, “Compression Multimodal Learning for Reconstruction of Temperature Field from Sparse Measurements in a Liquid Metal Cooled Reactor,” (in preparation, to be submitted to Scientific Reports).
10. **L. Kohler**, A. Heifetz, M. Weathered, and A. Cilliers, “LSTM Autoencoder Prediction of Distributed Temperature in Liquid Sodium using Measurements with Co-located Fiber Optic Sensor and Sparse Multi-Point Thermocouple Array,” in Transactions of American Nuclear Society. Washington, D.C., USA, November 12-15, 2023.
11. A. Furlong, F. Alsafadi, **L. Kohler**, X. Wu, S. Palmtag, A. Godfrey, and S. Hayes. “Machine Learning-Based Prediction of Crud Buildup Locations in Pressurized Water Reactors,” in Transactions of American Nuclear Society. Washington, D.C., USA, November 12-15, 2023.

© Copyright 2025 by Lauren Ashley Kohler

All Rights Reserved

Bayesian Calibration and Machine Learning-based Validation of Distributed Fiber Optic
Sensors for Advanced Temperature Sensing in Nuclear Reactors

by
Lauren Ashley Kohler

A thesis submitted to the Graduate Faculty of
North Carolina State University
in partial fulfillment of the
requirements for the Degree of
Master of Science

Nuclear Engineering

Raleigh, North Carolina
2025

APPROVED BY:

Dr. John Zino

Dr. Igor Bolotnov

Dr. Xu Wu
Chair of Advisory Committee

DEDICATION

To my father, my greatest cheerleader, who always encouraged me to reach for the stars. His unwavering support and work ethic have been my guiding light, inspiring me to pursue higher education and always strive for excellence. He always told me, "*If the Eagles could win the Super Bowl, then you can achieve anything you set your mind to.*" And he was right, twice.

BIOGRAPHY

Lauren Kohler was born in Elizabeth City, NC, and raised on a farm in rural Hobbsville, NC. She attended the North Carolina School of Science and Mathematics in Durham, NC, for her junior and senior years of high school, where she developed a strong foundation in mathematics, taking advanced courses in graph theory and combinatorics. Her early interest in problem-solving and mathematical modeling laid the groundwork for her future studies in engineering.

In August 2020, Lauren began her undergraduate education at North Carolina State University, where she pursued a Bachelor of Science in Nuclear Engineering with a minor in Mathematics. Throughout her undergraduate years, she became involved in research and professional development opportunities that shaped her academic and career trajectory. She joined the Artificial Intelligence for Simulations of Advanced Nuclear Systems (ARTISANS) group under Dr. Xu Wu, where she was introduced to uncertainty quantification and machine learning methodologies. Her work in this group focused on applying artificial intelligence to enhance simulations and data-driven modeling in nuclear engineering.

Seeking to expand her research experience, Lauren was selected for a Science Undergraduate Laboratory Internship (SULI) at Argonne National Laboratory in January 2023, working under Dr. Alexander Heifetz. During this appointment, she conducted research on fiber optic temperature sensors for advanced reactor applications, an area that became central to her master's thesis. She also gained valuable industry experience through two internships at General Electric Hitachi (GEH) in Wilmington, NC, during the summers of 2022 and 2024, where she worked on nuclear reactor design and optimization projects.

At the time of writing, Lauren has presented her research at eight conferences, co-authored an opinion piece, and submitted two journal papers. Her contributions to the field include advancements in machine learning applications for nuclear reactor monitoring and uncertainty quantification techniques for sensor validation. She has also been actively involved in professional societies, outreach initiatives, and mentorship programs, aiming to encourage more students, particularly women, to pursue careers in nuclear science and engineering.

Currently, Lauren is completing her Master of Science in Nuclear Engineering under the University Nuclear Leadership Program (UNLP) fellowship. Upon graduation, she plans to participate in the Edison Engineering Development Program at GEH, a two-year leadership program designed to cultivate technical and leadership skills. In parallel, she will be pursuing a doctoral degree in nuclear engineering at NC State, where she aims to continue her research on Artificial Intelligence and Machine Learning for advanced reactor modeling.

ACKNOWLEDGEMENTS

I would like to express my deepest gratitude to Dr. Xu Wu for his invaluable mentorship throughout my academic journey. His guidance has been instrumental in shaping my understanding of nuclear engineering and machine learning, providing critical support through both my undergraduate and graduate studies. I am sincerely grateful to Dr. Alexander Heifetz of Argonne National Laboratory for his mentorship and for introducing me to this research. I also appreciate Argonne National Laboratory for providing the experimental data from the Mechanisms Engineering Test Loop (METL) facility. Special thanks to Matthew Weathered for his assistance in interpreting and analyzing the data.

I extend my appreciation to the board members for their insightful feedback throughout this study. Their engagement and thoughtful advice have helped guide and refine my research. I would also like to acknowledge the University Nuclear Leadership Program (UNLP) for supporting my graduate education through a fellowship, allowing me the opportunity to fully dedicate myself to my studies and research. I am grateful to the members of ARTISANS for their collaboration and for continuously challenging me to expand my knowledge of machine learning in the nuclear field. Their curiosity, expertise, and support have provided an environment that fosters both learning and growth.

Beyond academia, I am incredibly thankful for my close friends—Samantha Watson, Eirini Klemes, Addyson Hunsicker, Abigail Davis, and Amy Whitley—who have given me inspiring examples of strong women in engineering to look up to, as well as study partners I could always rely on. Their encouragement and camaraderie have made this journey more meaningful. I am especially thankful to my partner, Jacob Watkins, for his patience, unwavering support, and belief in me throughout this process. Lastly, a special thanks to my dachshund, August, for his companionship and comfort during the long hours of research and writing.

To all who have supported and inspired me, I am truly grateful.

TABLE OF CONTENTS

List of Tables	vii
List of Figures	viii
Chapter 1 INTRODUCTION	1
1.1 Sensors in Nuclear Systems	2
1.2 Motivation	5
1.3 Problem Definition and Goals	6
1.4 Thesis Outline	7
Chapter 2 METHODOLOGIES	9
2.1 Fiber Optic Cables for Sensing	10
2.2 Data Acquisition	11
2.2.1 Case Study 1: Water Mixing Tee	11
2.2.2 Case Study 2: Liquid Sodium THETA	13
2.3 Inverse Uncertainty Quantification	17
2.4 Sensitivity Analysis Methods	19
2.4.1 Correlation Coefficient	19
2.4.2 Morris Method	20
2.4.3 Sobol Indices	21
2.5 Machine Learning for Validation	22
2.5.1 Autoencoders	23
2.5.2 LSTM Networks	24
Chapter 3 CASE STUDY 1: WATER MIXING TEE RESULTS	26
3.1 Bayesian Calibration	27
3.2 Importance Ranking	29
3.3 Validation	33
Chapter 4 CASE STUDY 2: LIQUID SODIUM THETA RESULTS	37
4.1 Bayesian Calibration	38
4.2 Importance Ranking	41
4.3 Validation	45
Chapter 5 CONCLUSIONS	49
5.1 Summary of Results	49
5.2 Conclusions	50
5.3 Future Work	51
References	53
APPENDICES	59
Appendix A list of Acronyms	60

Appendix B List of Symbols and Variables 62

LIST OF TABLES

Table 3.1	Results obtained through sampling using DRAM to estimate the parameters with the initial values given alongside the posterior means, standard deviation, error with Monte Carlo sampling and other metrics.	29
Table 4.1	Parameter estimates derived from DRAM sampling, comparing initial values with posterior means, standard deviations, Monte Carlo sampling error, and additional statistical metrics.	41
Table 4.2	The total training time on the LSTM autoencoder by running on an M1 Apple chip with the ending RMSE.	47
Table 4.3	Error metrics in °C for predictions using an LSTM Autoencoder trained on different data combinations, compared against spline interpolation errors. Spline interpolation errors are included as a reference for comparison. . .	48
Table A.1	A summary of acronyms used in alphabetical order.	60
Table B.1	A summary of common meteorological variables and their abbreviations in alphabetical order.	62

LIST OF FIGURES

Figure 2.1	Piping and instrumentation diagram of a flow loop containing a mixing tee. Various components are outlined including a circulation pump, a heater, flow meters, and locations of the thermocouples (TC).	12
Figure 2.2	Flow rate of the total and cold coolant within the flow loop during tests.	13
Figure 2.3	[Left] Diagram of THETA with main components denoted. [Right] Image of THETA captured from Argonne National Laboratory.	14
Figure 2.4	Diagram of primary and secondary loop of THETA with the temperature discretion shown in THETA between the hot and cold pool.	15
Figure 2.5	Cross section of THETA with the heater, pump, and IHX represented. The location of the co-located multi-array thermocouples and distributed fiber optic cables illustrated.	16
Figure 2.6	Temperature distribution measured in THETA during thermal stratification transient using co-located multi-point thermocouple temperature sensors.	16
Figure 2.7	Visualization of Bayesian statistics with a synthetic distribution.	18
Figure 2.8	Outline of a one-layer neural network with a representation of the activation function to obtain the outputs.	23
Figure 2.9	Simple diagram of an autoencoder showing the compression of inputs and decoding to obtain the outputs.	24
Figure 2.10	A diagram of a LSTM memory cell with its key gating mechanisms.	25
Figure 2.11	Layout of the LSTM autoencoder for validation of DFOS using input from thermocouples.	25
Figure 3.1	Chain plots obtained after 100,000 samples using DRAM with a 5,000 burn-in to approach convergence for the distribution.	28
Figure 3.2	Auto-correlation plot as a function of lags to show the dependence of each sample proposition on the previous sample.	29
Figure 3.3	A distribution, correlation plot and contour plot of the parameter propositions as obtained through DRAM.	30
Figure 3.4	Residual error between the DFOS and thermocouple array within the flow loop comparing the prior parameters and the obtained parameters through DRAM for calibration of the parameters.	31
Figure 3.5	Pearson and Spearman correlation coefficients for each of the 4 co-located thermocouple sensors to determine the most important location for calibration purposes.	32
Figure 3.6	Results obtained of μ and σ from applying Morris method to the co-located temperature sensors within the mixing loop.	32
Figure 3.7	The total, first, and second order effects for the co-located temperature sensors within the flow loop.	33

Figure 3.8	[Top] RMSE of the training of the LSTM autoencoder for validation of the DFOS through inputs of the thermocouples where the validation set and training set are denoted to show efficiency during training. [Bottom] Log RMSE plot to show more more minute changes.	34
Figure 3.9	Residual error between the predicted temperature obtained from the LSTM auto encoder and measured thermocouple temperature from the flow loop. The training, validation, and testing set are shown over the test.	35
Figure 3.10	Error between the prediction found from the LSTM autoencoder and the temperature measurement from the distributed fiber optic temperature sensors.	36
Figure 4.1	Chain samples obtained through DRAM methodology from data in THETA.	39
Figure 4.2	Distribution from the samples obtained through DRAM with more detail shown in pair plots in the bottom diagonal and contour plot shown in the upper diagonal.	39
Figure 4.3	Autocorrelation plot of the estimated parameters in the calibration curve of the distriubted fiber optic sensors in THETA.	40
Figure 4.4	Cumulative explained variance of the thermocouple sensors necessary to have an accurate display of the axial range to reduce the total input size.	42
Figure 4.5	Peason and Spearmann correlation for each of the co-located sensors at 20 different axial locations.	42
Figure 4.6	Morris method results at 3 different locations for the co-located sensors with each of the axial location denoted. Due to the low standard deviation of obtained from the method, a scale of 1000 is applied to show the magnitude.	43
Figure 4.7	The first and total effects obtained from Sobol indices at the different locations for the co-located sensors.	44
Figure 4.8	A detailed diagram showing results from the training loss with the validation loss also shown when training on 2 of the 3 co-located sensors. . .	45
Figure 4.9	Comprehensive diagram of the error obtained when comparing the predicted temperature data and the measured DFOS. The top plots show the error over the 520 axial sensing location. A comparison is shown between predicting the temperature when using interpolation methods. A density distribution of the residual is shown in the bottom row of the figure. . . .	46

CHAPTER

1

INTRODUCTION

Nuclear reactors are currently undergoing extensive development to provide a more sustainable and efficient source of power, contributing to global de-carbonization efforts (Omar et al. 2022). Most reactors on the current energy grid operate as Generation III systems, including pressurized water reactors (PWRs) and boiling water reactors (BWRs) (Marques 2011). While these reactors have demonstrated reliability and safety, improvements are being explored to enhance public perception and reduce capital costs, making nuclear power more competitive with other energy sources (Mignacca et al. 2020).

Advanced reactor designs, including Generation IV reactors, address several challenges associated with existing nuclear technology (Zohuri 2020). Among these, sodium-cooled fast reactors (SFRs) (Aoto et al. 2014) and molten salt-cooled reactors (MSCRs) (Serp et al. 2014) offer significant advantages by utilizing alternative coolants and fuel cycles, leading to improved thermal efficiency and enhanced fuel utilization (Zinkle et al. 2016; Arostegui and Holt 2019). These reactors operate at higher temperatures and often incorporate passive safety features (Nayak and Sinha 2007), reducing the risk of core damage while enabling longer intervals between refueling cycles (Corkhill et al. 2025).

One of the key benefits of these advanced reactor designs is the potential for more efficient fuel burnup, which reduces the volume of long-lived radioactive waste (György and Czifrus 2015). Additionally, their ability to operate at ambient pressure decreases the structural re-

quirements for reactor vessels, lowering construction costs (Yvon and Carré 2009). However, the economic viability of these reactors depends on optimizing operating and maintenance (O&M) costs, particularly in monitoring and control systems (Jin and Bang 2024; Abou-Jaoude et al. 2023). Implementing advanced sensing technologies, such as distributed fiber optic sensors (DFOS), can aid in reducing O&M costs. Fiber optic sensors can provide high-resolution temperature data for real-time monitoring and early fault detection, improving reactor safety and operational efficiency.

It is integral for the nuclear industry to continue to push towards automation. One method of modernization is by incorporating advanced instrumentation and machine learning-driven monitoring strategies. Use of this technology can further improve reactor performance, reduce downtime, and enhance predictive maintenance capabilities (Kovesdi et al. 2021; Alberti et al. 2023). The successful deployment of these technologies will be critical in ensuring that next-generation reactors can deliver clean, cost-effective, and reliable energy to meet future demands.

1.1 Sensors in Nuclear Systems

Temperature measurement is a critical aspect of reactor monitoring ensuring both safety and efficiency (Korsah et al. 2016). In nuclear reactors, even minor temperature fluctuations can impact thermal-hydraulic performance, fuel integrity, and overall reactor stability. Accurate and reliable temperature sensing is essential for maintaining optimal operating conditions, preventing overheating, and detecting potential failures before they escalate. By continuously monitoring temperature, reactor operators can make informed decisions that improve reactor efficiency, extend component lifespan, and enhance overall safety. Temperature sensors provide essential data that help maintain operational stability and allow for proactive maintenance, preventing costly shutdowns and ensuring the long-term sustainability of nuclear energy production. Without precise temperature monitoring, reactors would be more vulnerable to localized overheating, material degradation, and inefficiencies in heat transfer, which could compromise safety and economic viability.

Traditionally, nuclear reactors rely on thermocouples as the primary temperature sensors (Hashemian and Jiang 2009). These devices consist of two dissimilar metal wires joined at one end, generating a voltage in response to temperature differences (Wu 2018). Thermocouples are widely used because of their simplicity, reliability, and well-established performance in high-temperature environments (Rempe et al. 2009). They provide real-time temperature readings at critical reactor components such as the core, coolant channels, and heat exchangers. However, thermocouples have several inherent limitations. One of their primary drawbacks is

that they provide only pointwise temperature measurements, meaning they can only capture temperature at specific, pre-determined locations (Reales Gutiérrez et al. 2024). This limitation makes it difficult to monitor temperature variations across larger reactor components, potentially missing localized hot spots or transient fluctuations that could indicate emerging operational issues. As a result, numerous thermocouples must be installed throughout the reactor to achieve comprehensive temperature monitoring, leading to increased complexity in system design and maintenance.

Another significant challenge associated with thermocouples is their susceptibility to degradation over time due to exposure to extreme reactor conditions (Kumar et al. 2025). Corrosion, embrittlement, and chemical interactions with reactor coolants can lead to sensor drift, requiring frequent recalibration and replacement. This is particularly problematic in advanced reactors that operate with high-temperature liquid-metal or molten salt coolants, where thermocouples degrade even more rapidly (Palmer et al. 2015). The frequent need for replacements increases O&M cost, especially in reactors where sensor maintenance requires a complete system shutdown or the use of specialized robotic systems (Stewart and Shirvan 2022). Additionally, thermocouples require multiple penetrations through the reactor vessel's pressure boundary to accommodate different sensing locations (Hyer et al. 2023). Each penetration introduces a potential point of structural weakness and increases the risk of leaks, which can compromise reactor safety (Hyvärinen et al. 2022). The complexity and cost of installing and maintaining thermocouples, combined with their limitations in providing spatially resolved temperature data, highlight the need for a more advanced sensing technology that can withstand harsh reactor environments while delivering more comprehensive thermal monitoring.

An alternative to conventional thermocouples is fiber optic sensors, which offer several advantages in nuclear reactor applications (Wu et al. 2021a; Davydov et al. 2019). These sensors operate based on changes in optical properties, such as light scattering and transmission, that occur in response to temperature fluctuations along the length of the fiber (Udd and Spillman Jr 2024). Unlike thermocouples, fiber optic sensors do not rely on metallic components, making them more resistant to corrosion, oxidation, and mechanical wear. Fiber optics have already been widely adopted in industries requiring high-precision sensing, including aerospace, structural health monitoring, and telecommunications (Rovera et al. 2023; Wu et al. 2020; Huang et al. 2019). In nuclear power, fiber optic sensors can be used for distributed temperature sensing (DTS), where an optical fiber functions as a continuous temperature sensor rather than a discrete point sensor (Lu et al. 2019). This allows for significantly higher spatial resolution in temperature measurements, providing a more detailed understanding of thermal behavior within the reactor. By enabling continuous monitoring along the entire length of a fiber, these sensors allow operators to track temperature variations with unprecedented accuracy,

capturing transient thermal events that would otherwise be undetectable with traditional thermocouple systems (Lenner et al. 2019).

One of the most significant advantages of fiber optic sensors over thermocouples is their reduced need for penetrations through the reactor vessel. While thermocouples require multiple insertion points for distributed temperature monitoring, fiber optics need only a single inlet and outlet penetration. This reduction in penetrations improves the structural integrity of the reactor vessel, decreases the risk of coolant leaks, and simplifies installation and maintenance. By minimizing the number of pressure boundary intrusions, fiber optic sensors enhance reactor safety and reliability while also reducing engineering challenges associated with maintaining a containment structure. Additionally, because fiber optic cables are highly flexible and can be routed through complex geometries, they can be strategically placed to provide optimal thermal coverage without requiring invasive modifications to the reactor design.

Fiber optic sensors are far more resistant to degradation in harsh reactor environments compared to thermocouples (Girard et al. 2019). Their silica-based structure is less susceptible to chemical interactions, and they do not contain metallic junctions that can corrode or weaken over time. As a result, fiber optics have a significantly longer operational lifespan, reducing the frequency of replacements and lowering overall maintenance costs. In reactors where sensor replacement is costly and complex, the long-term durability of fiber optic sensors provides a major economic benefit. The extended operational lifetime of fiber optics also translates into fewer disruptions in reactor operation, as they require less frequent intervention for calibration and maintenance. This increased reliability ensures that continuous and accurate temperature data is available without the need for frequent shutdowns or labor-intensive replacements, making fiber optic sensors an attractive choice for next-generation reactor monitoring systems.

Unlike thermocouples, which provide discrete temperature measurements at fixed locations, fiber optic sensors enable continuous, high-resolution temperature mapping along the entire length of the fiber (Lu et al. 2019). This capability is particularly valuable in advanced reactor designs, where precise temperature control is essential for maintaining efficient heat transfer and detecting localized thermal anomalies. With fiber optics, operators can monitor subtle temperature variations that might otherwise go unnoticed with traditional pointwise sensors. This level of spatial resolution provides a more in-depth view of reactor thermal behavior, allowing for early detection of potential failures, optimization of coolant flow, and improved overall reactor efficiency. Continuous monitoring also enhances safety margins by enabling real-time detection of abnormal temperature gradients that could indicate structural issues or coolant flow disruptions. The ability to track these variations with high accuracy makes fiber optic sensors an indispensable tool for improving reactor performance and extending component lifespan.

Although the initial installation costs of fiber optic sensors may be comparable to those of thermocouple networks, the long-term savings in maintenance, replacement, and labor costs make fiber optics a more cost-effective solution. The reduced need for penetrations, combined with the longevity of the sensors, minimizes operational disruptions and reactor downtime, leading to overall cost reductions in nuclear plant operation. Additionally, because fiber optic sensors can be integrated into existing reactor monitoring systems with minimal modifications, they provide a scalable and adaptable solution that can be deployed across different reactor designs. As fiber optic technology continues to advance, its potential applications in nuclear energy will expand, further solidifying its role as a superior alternative to conventional temperature measurement systems.

While fiber optic sensors provide high-fidelity temperature data, one of the main challenges lies in processing and interpreting this information efficiently (Huang et al. 2021; Ghafoori et al. 2020). Unlike thermocouples, which generate simple numerical outputs at a limited number of points, fiber optics produce large, continuous datasets that require analytical methods to extract meaningful insights. Managing these data streams is essential for maximizing the benefits of fiber optic sensing technology. Developing effective data processing techniques will be crucial for fully integrating fiber optics into reactor monitoring systems. By improving data interpretation, reactor operators can leverage fiber optic sensors to enhance real-time temperature monitoring, detect anomalies earlier, and optimize reactor performance. Continued research in this area will ensure that fiber optic technology becomes a key component of next-generation nuclear reactor safety and efficiency.

The integration of fiber optic sensors in nuclear reactors represents a significant step forward in temperature monitoring technology. Their ability to provide high-resolution, continuous temperature data, combined with increased durability and fewer penetration points, makes them a superior alternative to traditional thermocouples. While challenges remain in processing and analyzing the vast amounts of data they generate, advancements in data interpretation methods can allow further use of DFOS.

1.2 Motivation

In the operation of a nuclear reactor, it is necessary to measure the temperature accurately. DFOS present an alternative to traditional thermocouples by offering high-resolution, continuous temperature data along the entire length of the fiber. However, the relationship between the raw DFOS readings and actual temperature values must be better understood to ensure accuracy and reliability. The calibration of DFOS temperature measurements requires the development of a correlation between the fiber optic response and the true thermal state of

the reactor environment. By refining this calibration curve, it becomes possible to extract meaningful temperature information from DFOS with greater confidence, allowing them to serve as a primary monitoring system rather than a supplementary one.

A key motivation for this work is the potential to reduce the number of thermocouples installed within the reactor, which are currently treated as the temperature truth for calibration and monitoring. While thermocouples provide reliable pointwise temperature measurements, they have inherent drawbacks, including limited spatial resolution, susceptibility to degradation, and the requirement for multiple penetrations through the reactor vessel. These penetrations introduce structural vulnerabilities and increase the likelihood of coolant leaks, while the frequent need for sensor replacement adds to O&M costs, particularly during refueling outages. If DFOS readings can be reliably validated and corrected, reactors could operate with fewer thermocouples, reducing these associated costs and streamlining reactor design without compromising safety or monitoring capabilities.

Additionally, ensuring the long-term reliability of DFOS requires a systematic approach to validating their readings against known temperature conditions. While DFOS offers high-resolution spatial data, they remain susceptible to environmental factors such as radiation exposure, mechanical strain, and signal drift, all of which can impact their accuracy. By comparing DFOS data with trusted thermocouple measurements, this work seeks to establish reliable methods for detecting and correcting sensor malfunctions. Understanding the conditions under which DFOS readings deviate from expected values will enhance the predictive capabilities of reactor monitoring systems, allowing operators to identify failing sensors before they impact reactor safety or performance. Developing strategies to recognize and account for sensor drift or degradation will improve the feasibility of widespread DFOS adoption in nuclear reactors, ensuring that these sensors remain a cost-effective and dependable solution for real-time temperature monitoring.

1.3 Problem Definition and Goals

A key challenge in deploying DFOS for reactor temperature monitoring is calibration, as these sensors do not inherently provide absolute temperature readings and must be referenced against known measurements. Thermocouples are currently used as the temperature truth, but reducing the number of thermocouples needed while maintaining accurate monitoring is essential for lowering O&M costs. This requires determining the optimal placement of thermocouples to establish a reliable calibration curve for DFOS while minimizing disruptions to reactor operation. The calibration process must refine the relationship between DFOS signal response and actual temperature, ensuring the accuracy of thermal measurements across

varying reactor conditions. By improving the calibration framework, DFOS can provide meaningful and consistent temperature data while reducing the need for extensive thermocouple networks.

Beyond calibration and sensitivity analysis (SA) are necessary to quantify the impact of various factors on DFOS performance, such as sensor placement, thermal gradients, and environmental conditions. Since DFOS provide distributed temperature measurements rather than discrete pointwise data, their readings are influenced by local temperature variations, signal attenuation, and mechanical strain. Use of SA will help determine which parameters most affect DFOS accuracy and how uncertainties in calibration propagate through the measurement system. Understanding these influences will enable refinement of the DFOS temperature conversion model, ensuring its robustness across different reactor environments. By identifying the most critical factors affecting DFOS performance, SA will provide insights into improving measurement accuracy and optimizing sensor placement for long-term reliability.

Validation is crucial for ensuring that DFOS remain accurate and reliable over extended periods of reactor operation. Unlike thermocouples, which provide stable pointwise measurements, DFOS readings can drift due to radiation exposure, mechanical stress, and thermal cycling, leading to long-term signal degradation. A systematic validation framework is required to detect deviations in DFOS readings and distinguish between normal temperature variations and sensor malfunctions. This involves cross-referencing DFOS data with thermocouple measurements to establish thresholds for acceptable deviations and implementing correction mechanisms to maintain sensor accuracy. By developing a validation methodology, DFOS can be integrated into reactor monitoring systems with confidence, ensuring they provide continuous, high-resolution temperature data while reducing reliance on conventional sensors.

The main goals of this work are to (1) establish an accurate calibration framework to ensure DFOS readings reliably correspond to true reactor temperatures, (2) conduct SA to determine the key factors influencing DFOS performance and improve the temperature conversion model, and (3) develop a validation methodology to detect and correct deviations in DFOS measurements, ensuring long-term reliability in nuclear reactor environments. By achieving these objectives, this research will enable the effective integration of DFOS into reactor monitoring systems, reducing the need for thermocouples and lowering O&M costs while maintaining accurate and high-resolution temperature monitoring.

1.4 Thesis Outline

This thesis is organized as follows: Chapter 2 introduces the methodology, with Section 2.2 detailing the experimental data acquisition, including measurements from a water-cooled

mixing tee flow loop and the THETA liquid sodium mockup. Sections 2.3, 2.4, and 2.5 outlines the numerical approaches used, including Delayed Rejection Adaptive Metropolis (DRAM) for Bayesian calibration, SA, and neural network models, specifically a Long Short-Term Memory (LSTM) autoencoder. Chapter 3 presents the results from the mixing tee flow loop, while Chapter 4 discusses the findings from the THETA experiment. Finally, Chapter 5 concludes the paper by addressing study limitations and potential improvements for future research.

CHAPTER

2

METHODOLOGIES

This study evaluates time-dependent datasets using parameter calibration techniques, SA, and machine learning validation models to offer an approach to interpreting thermal behavior. The datasets were collected at Argonne National Laboratory from two distinct experimental systems within the Mechanisms Engineering Test Loop (METL). These experiments represent approaches for gathering high-fidelity fiber optic thermal hydraulic data and thermocouple temperature data. Section 2.2 details the two experimental setups analyzed in this study. Specifically, Section 2.2.1 focuses on the baseline experiment, where thermal mixing phenomena in a water mixing tee were examined. In this setup, water served as the working fluid, and a 38 kW electrical pump was used to circulate the fluid while a heater operated over time to collect temperature data. Section 2.2.2 delves into the Thermal Hydraulic Experimental Test Article (THETA), which used liquid sodium as the working fluid. In both setups, thermocouples and fiber optic cables were employed to capture temperature measurements.

Subsequent sections describe the methodologies applied to analyze the collected data. Section 2.1 describes the fiber optic cables used in following sections alongside a description of the scientific background of this component. Section 2.3 explains the use of inverse uncertainty quantification (IUQ) for calibrating the fiber optic system parameters, with a focus on the implementation of the MCMC DRAM algorithm. Section 2.4 outlines various SA methods used to rank measurement locations, facilitating sensor reduction for future applications. Finally,

Section 2.5.2 describes the machine learning techniques employed in this study, specifically the use of a LSTM autoencoder. This model was used to resize fiber optic data to match thermocouple data, enabling comparisons to determine the accuracy and functionality of the fiber optic system.

2.1 Fiber Optic Cables for Sensing

Fiber optic cables are a tool in advancing temperature sensing technologies with high spatial resolution and reduced need for intrusive penetrations in reactor pressure boundaries. Their capability to provide continuous, distributed temperature measurements makes them particularly well-suited for applications in advanced reactors. This study investigates their use for monitoring temperature fields in high-temperature environments.

The fundamental principle of fiber optic temperature sensing relies on the interaction between light and the fiber's material properties. Different types of scattering processes occur within the optical fiber, each offering unique advantages for sensing applications. Rayleigh scattering, a linear scattering phenomenon caused by microscopic inhomogeneities in the fiber's material, is the primary mechanism responsible for signal attenuation in optical fibers (Young 1981). It also enables backscatter-based temperature sensing, where frequency shifts in the backscattered light are used to infer temperature changes. In contrast, Brillouin scattering involves nonlinear interactions that generate frequency shifts based on temperature- and strain-induced variations in the fiber (Wolff et al. 2021). Although Brillouin scattering can be used for distributed temperature sensing, its low amplitude often limits its practicality in harsh environments. Raman scattering, another nonlinear process, is particularly sensitive to temperature changes and is widely employed in DTS systems for nuclear applications (Langer et al. 2019). Similar to Brillouin scattering, Raman scattering also faces challenges with a low amplitude.

In this study, a single-mode optical fiber with a wavelength of 1550 nm was used, interrogated by the Luna Optical Distributed Sensor Interrogator (ODiSI 6000). The setup leverages Rayleigh scattering to measure temperature along the fiber's length (Kautzman et al. 2018; Korganbayev et al. 2020). The fiber optic cable, housed within stainless steel capillary tubes for protection, provides high-resolution measurements with spatial intervals of 2.6 mm (Benoit and Yappert 1996). This configuration allows for use at an elevated temperature, which is similar to that of nuclear reactor environments. These sensors are then calibrated using co-located thermocouple arrays.

2.2 Data Acquisition

To support the development and validation of temperature field reconstruction methodologies, data was acquired from two experimental systems: the thermal mixing tee and the THETA. Each system offers unique insights into temperature behavior under different operational conditions.

The thermal mixing tee discussed in Section 2.2.1 investigates the behavior of thermal mixing in liquid water systems. This setup experienced multiple transient events during testing, allowing for the observation of dynamic thermal interactions and heat transfer mechanisms. These transients provide a rich dataset for understanding the response of the system to varying flow and thermal conditions.

THETA is a reactor-grade sodium test facility designed to study thermal hydraulic phenomena with liquid sodium as the working fluid. Section 2.2.1 explains more in detail the experiments conducted in THETA focused on thermal stratification, capturing the development and evolution of temperature layers over time. High-resolution temperature measurements were obtained using co-located thermocouple arrays and fiber optic sensors.

Together, the data from these systems provide a proposition for this methodology with validating advanced temperature reconstruction methods. The combination of transient thermal mixing data and stratification measurements offers a dataset for exploring spatiotemporal temperature dynamics in liquid metal environments.

2.2.1 Case Study 1: Water Mixing Tee

In the first case study, fiber optics measured the temperature in a thermal mixing tee where the working fluid was water. The flow loop containing the fluid mixing tee is located in METL at Argonne National Laboratory, where Figure 2.1 shows the piping and instrumentation diagram. A similar setup has been used in other studies, such as the investigation of thermal mixing and flow transients in a water loop, where thermocouples and DFOS were co-located to monitor temperature distributions in a nearly identical experimental design (Ankel et al. 2020, 2021; Pantopoulou et al. 2022). The tube material within the flow loop is made using polycarbonate piping throughout the system. The fluid flows in a clockwise manner such that the flow travels in an anti-gravity function through the mixing tee. The fluid speed is changed by the use of a 1.5 HP stainless circulation pump located towards the bottom left as shown in Figure 2.1. After pumping through the circulation pump, some of the fluid travels through the “hot leg”. This fluid is heated using a variable 4000 W Watlow FLC-16 electric heater. The other flow continues through the “cold leg”. Both the “hot leg” and “cold leg” fluid are mixed together as indicated by the left side of Figure 2.1. Thermocouples are located prior to the mixing in the “hot leg” and

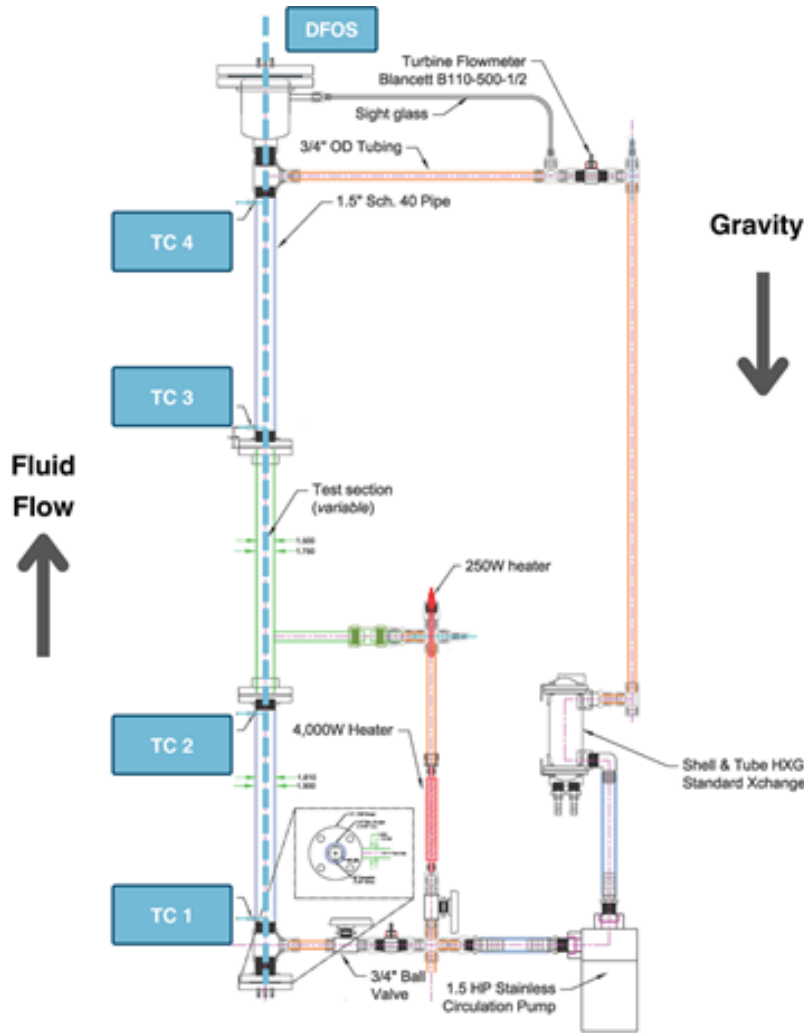


Figure 2.1: Piping and instrumentation diagram of a flow loop containing a mixing tee. Various components are outlined including a circulation pump, a heater, flow meters, and locations of the thermocouples (TC).

“cold leg”. In addition, another thermocouple is located about 23 inches after the mixing of the two fluids. The fluids are brought back to room temperature using a 130,000 BTU shell and tube heat exchanger with a coupled 11,300 BTU/hr chiller McMaster 3531K12. A fiber optic cable is threaded through the left most piping of Figure 2.1. This obtains measurement data from the cold leg and the mixed fluid data.

In the water test, measurements are taken every second over a period of about 2100 seconds. A total of 7 different flow rates occur over the timing due to changing the circulation pump speed, all of which reach steady state as shown in Figure 2.2. This figure shows the measured flow rates as detected in the cold leg and the fully mixed flow towards the top of the piping

where the flow meters have measuring accuracy of $\pm 1\%$ of the reading. Thermocouple Type K are used to measure the fluid within the “hot leg” and “cold leg”. These are chosen as they are typically used in nuclear applications due to the high radiation hardness. However, they do face challenges with the longevity of use. Thermocouple Type K can measure up to 1100°C with accuracy of $\pm 1.1^\circ\text{C}$. It is important to note that at time stamps prior to about 1000s experience higher levels of noise due to the high fluid flow.

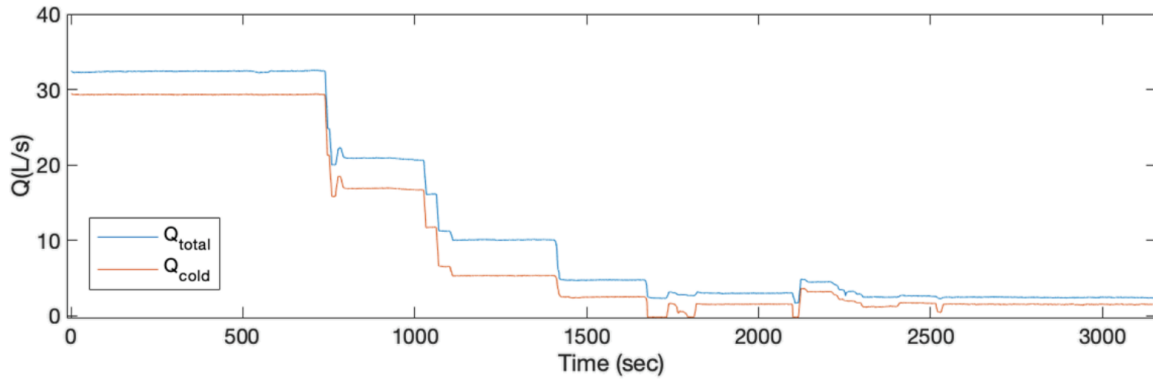


Figure 2.2: Flow rate of the total and cold coolant within the flow loop during tests.

2.2.2 Case Study 2: Liquid Sodium THETA

Case study 1 evaluates the use of this methodology with heated water as the coolant, representative of the conditions in the current operating nuclear reactor fleet, including PWRs and BWRs. In case study 2, the test facility employs liquid sodium as the coolant, simulating the conditions of a SFR for validating reactor thermal-hydraulic behavior. Experimental data for this case was collected from the THETA at Argonne National Laboratory. This facility is designed to replicate both nominal operational conditions and transient scenarios. In other studies, the same experimental setup has been utilized to monitor liquid sodium systems, such as in anomaly detection for cold trap operation at the METL at Argonne National Laboratory, where multisensory data fusion with LSTM autoencoders was applied to identify operational anomalies (Akins et al. 2023). Further details on the status and experimental validation of THETA can be found in the FY2019 report, which outlines the facility’s capabilities and contributions to sodium-cooled reactor technology (Weathered et al. 2019).

THETA comprises a primary and a secondary loop, with the primary system including a sodium pool containing an electrically heated core, a centrifugal pump, an intermediate heat

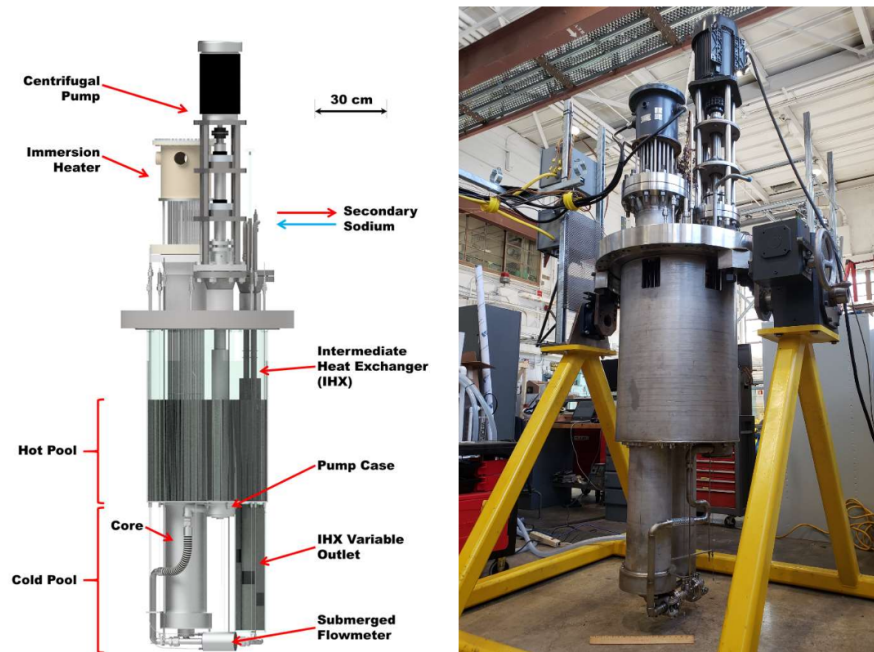


Figure 2.3: [Left] Diagram of THETA with main components denoted. [Right] Image of THETA captured from Argonne National Laboratory.

exchanger (IHX) interfacing with the secondary loop, and associated piping. The secondary system, located outside the sodium pool, features a sodium-to-air heat exchanger, a pump, and connecting piping and valves. A schematic representation of THETA, alongside a laboratory photograph, illustrates its physical configuration, including the vertical vessel design, immersion heater, and associated sodium flow paths, as shown in figure 2.3. The system is designed to operate under controlled conditions to study transient behaviors relevant to SFR operation.

A detailed piping and instrumentation diagram, depicted in figure 2.4, illustrates the primary and secondary flow loops within THETA, highlighting key components such as the immersion heater, IHX, pumps, and flow measurement locations. Sodium is circulated within the primary pool, where it is heated and subsequently transferred to the IHX. The secondary system extracts heat via the air heat exchanger, maintaining controlled thermal conditions for experimental validation. The sodium pool within the primary system has an outer diameter of 28 inches and a total height of 59.40 inches, ensuring sufficient thermal mass to study dynamic temperature gradients and stratification effects.

To facilitate experimental analysis, the vessel lid layout, shown in figure 2.5, provides an overhead view of the core system components. The primary heater, pump, and IHX are distinctly

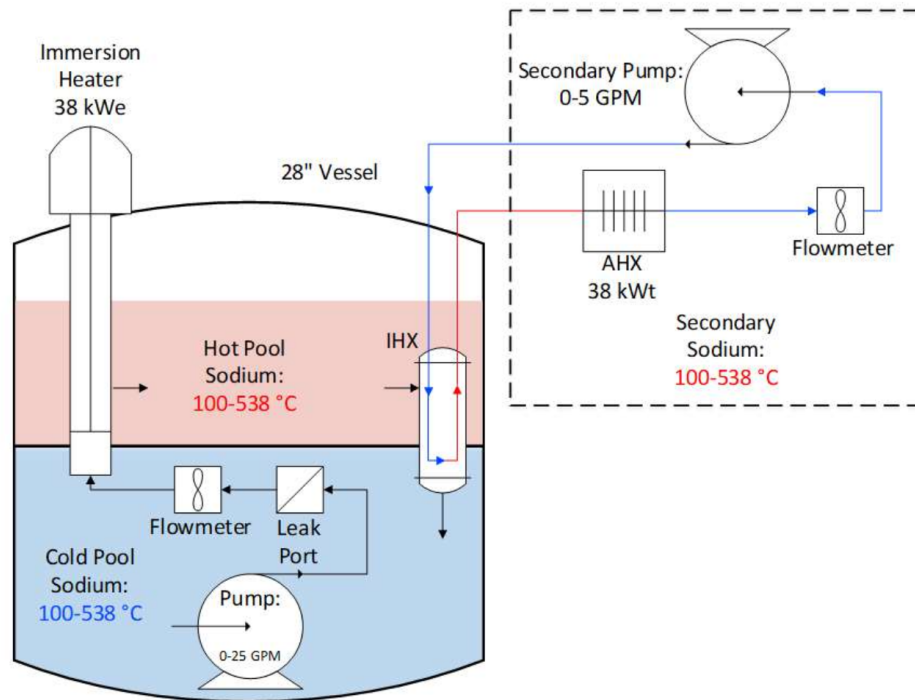


Figure 2.4: Diagram of primary and secondary loop of THETA with the temperature discretion shown in THETA between the hot and cold pool.

positioned to optimize thermal and flow distributions. Multiple instrumentation ports are arranged symmetrically around the vessel, allowing for precise temperature and flow rate measurements at various locations within the sodium pool. The instrumentation array consists of both thermocouples and fiber optic sensors, enabling high-resolution temperature profiling throughout the system. These sensors are placed to observe thermal stratification effects.

For this case study, a transient scenario was conducted to replicate thermal stratification within the sodium pool. The flow rate was maintained at 5 gallons per minute (GPM). Initially, the heater power was set to 0%, and at 120 seconds, it was activated to 51.4% duty cycle. The heater power was sustained at this level for 1000 seconds before being turned off, returning to 0% duty cycle. It is important to note that these tests were conducted using the old SSR controller, which lacked a power meter. Consequently, the electrical power supplied to the heater could only be estimated at approximately 20 kWe.

The transient response of the system, captured through high-frequency data acquisition, provided critical insights into the thermal behavior of the sodium pool. Figure 2.6 presents the temperature distribution within the pool at various time intervals, illustrating the development of thermal stratification over the course of the experiment. The upper region of the sodium pool exhibited a rapid increase in temperature following heater activation, while the lower

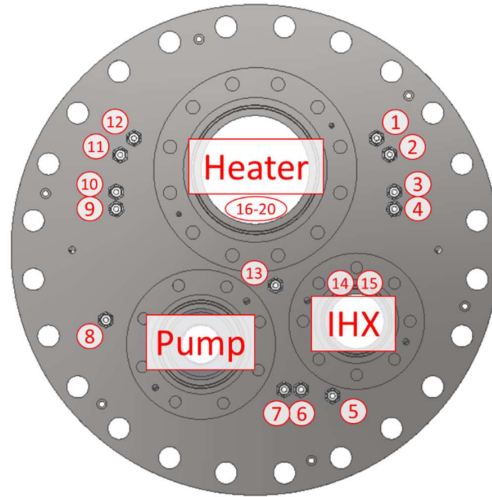


Figure 2.5: Cross section of THETA with the heater, pump, and IHX represented. The location of the co-located multi-array thermocouples and distributed fiber optic cables illustrated.

region experienced a delayed response, indicative of limited convective mixing.

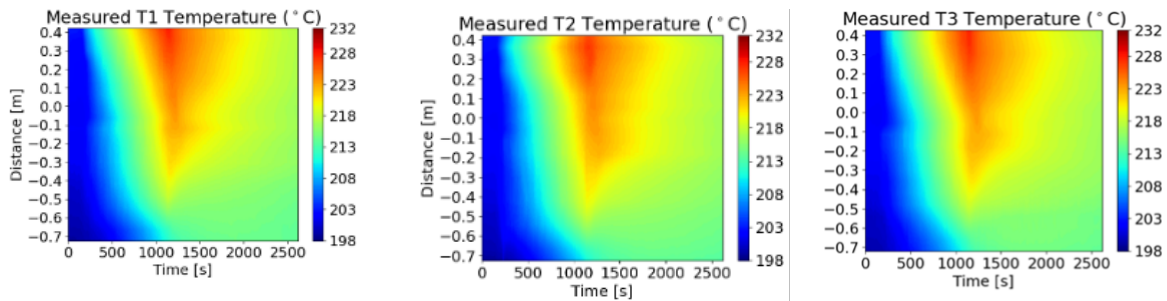


Figure 2.6: Temperature distribution measured in THETA during thermal stratification transient using co-located multi-point thermocouple temperature sensors.

In addition to temperature measurements, flow rate data collected during the transient test confirmed the stability of sodium circulation within the primary loop. The centrifugal pump maintained a consistent flow rate throughout the experiment, ensuring uniform heat transfer from the immersion heater to the bulk sodium. This steady-state operation is essential for benchmarking computational models used in reactor design and safety evaluations.

2.3 Inverse Uncertainty Quantification

Inverse uncertainty quantification (IUQ) is a process used to infer unknown parameters within a model based on observational data (Tarantola 2005; Wu et al. 2021b). This process is particularly useful in parameter calibration for complex systems where direct measurement or computation of certain parameters is infeasible. While forward uncertainty quantification (UQ) propagates known input uncertainties through a model to predict output uncertainty, IUQ identifies the underlying parameters that reproduce observed behaviors while accounting for uncertainty in both the data and the model itself. This approach ensures that parameter estimates remain consistent with physical realities and the inherent variability of experimental or operational environments.

A typical approach to IUQ involves formulating through Bayesian inference, where prior knowledge about parameters is combined with observational data to compute a posterior probability distribution. This is illustrated in Figure 2.7, which demonstrates the refinement of parameter estimates through IUQ using Bayesian inference (Stuart 2010; Wu et al. 2018a,b). The posterior, $p(\theta|\mathbf{y})$, is derived using Bayes' theorem as shown in Equation (2.1) where θ represents the unknown parameters, \mathbf{y} the observed data, $p(\mathbf{y}|\theta)$ the likelihood function quantifying the agreement between the model and data, and $p(\theta)$ the prior representing pre-existing knowledge about θ .

$$p(\theta|\mathbf{y}) \propto p(\mathbf{y}|\theta) \cdot p(\theta), \quad (2.1)$$

Inverse UQ often involves high-dimensional parameter spaces, requiring sophisticated numerical techniques to approximate the posterior and extract meaningful parameter estimates (O'Hagan 2006; Kennedy and O'Hagan 2001; Higdon et al. 2008).

Markov Chain Monte Carlo (MCMC) methods are useful in sampling from complex posterior distributions, especially when analytical solutions are impractical (Tierney 1994; Wu 2017). Among these, the DRAM algorithm can be performed using samples from MCMC results (Haario et al. 2006). DRAM improves upon the standard Metropolis-Hastings algorithm by employing delayed rejection, which generates alternative proposals when the initial move is rejected, thereby enhancing the exploration of the parameter space. Additionally, DRAM incorporates adaptive proposals, dynamically adjusting the covariance of the proposal distribution to better align with the shape of the posterior, accelerating convergence. Mathematically, DRAM's adaptation is expressed through the iterative update of the proposal covariance, Σ , as shown in Equation (2.2) where n is the iteration number, θ_i the sampled parameter vector at iteration i , and $\bar{\theta}$ the mean of the samples up to iteration n . This ensures that the chain adapts

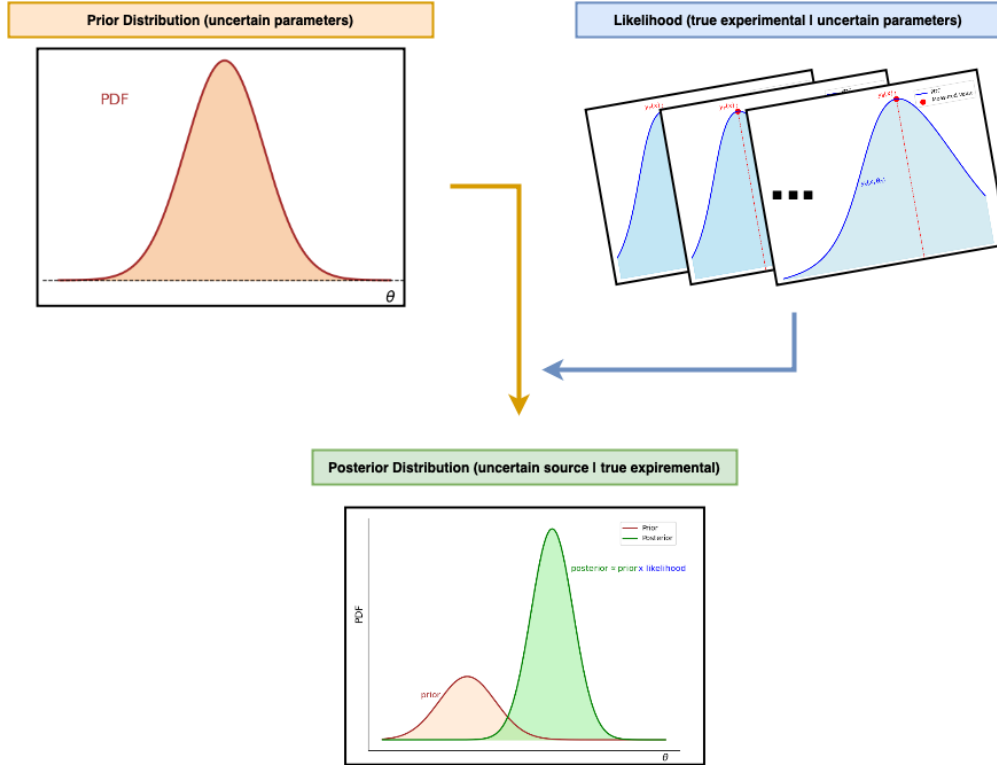


Figure 2.7: Visualization of Bayesian statistics with a synthetic distribution.

to the local posterior geometry, improving acceptance rates and reducing burn-in times.

$$\Sigma_{n+1} = \frac{1}{n} \sum_{i=1}^n (\theta_i - \bar{\theta})(\theta_i - \bar{\theta})^\top, \quad (2.2)$$

The convergence of the Markov chain within an MCMC algorithm indicates that the chain has reached a stationary distribution representative of the posterior. This is often assessed using diagnostics such as the autocorrelation function (ACF), which measures the correlation between successive samples in the chain. As the chain converges, the ACF decreases, indicating that successive samples are becoming less correlated and providing a more comprehensive exploration of the posterior. The effective sample size, derived from the ACF, is another key metric, as it quantifies the number of independent samples obtained despite correlations within the chain.

To further analyze MCMC results, pairwise plots of parameter distributions offer a visual representation of the parameter distributions. These plots illustrate the joint and marginal posterior distributions of parameter pairs, highlighting correlations and revealing the structure of the posterior landscape. For example, a Gaussian-shaped distribution in the pairwise plot indicates well-constrained parameters, whereas elongated or irregular shapes may suggest

strong correlations or multimodal posteriors. DRAM’s adaptive nature is particularly effective in resolving such challenges, as it dynamically reshapes the proposal distribution to improve sampling efficiency in these regions.

The efficiency of DRAM in practice is evident in its ability to generate reliable parameter estimates with fewer iterations compared to non-adaptive MCMC methods. By employing delayed rejection, the algorithm avoids becoming trapped in local minima, ensuring robust exploration of the parameter space. The effectiveness of this approach can be observed in Figure 2.7, which presents the posterior distributions of the calibrated parameters along with their pairwise correlations, demonstrating improved parameter convergence and reduced estimation uncertainty.

2.4 Sensitivity Analysis Methods

Sensitivity analysis (SA) is a critical tool in modeling and simulation, used to quantify the influence of input parameters on a model’s outputs. By systematically varying inputs, SA identifies the most impactful parameters, highlights potential interactions, and assesses the robustness of a system under uncertainty. This process aids in refining models, prioritizing data collection efforts, and guiding decision-making. Sensitivity analysis is typically divided into two categories: local sensitivity analysis (LSA), which examines the effect of small perturbations near a baseline point, and global sensitivity analysis (GSA), which evaluates the entire input space to capture non-linearities and interactions among parameters (Saltelli et al. 2008; Wainwright et al. 2014; Iooss and Lemaître 2015). This distinction ensures that SA can address diverse modeling needs, from initial screening of influential variables to comprehensive understanding of complex systems.

2.4.1 Correlation Coefficient

Correlation coefficients are used to identify the relationship between input variables and model outputs. The Pearson Correlation Coefficient (PCC) measures the strength and direction of a linear relationship between an input parameter X_i and output Y . Mathematically, it is defined in Equation (2.3) where $\text{Cov}(X_i, Y)$ is the covariance between X_i and Y , and σ_{X_i} and σ_Y are the standard deviations of X_i and Y , respectively.

$$\rho_{X_i, Y} = \frac{\text{Cov}(X_i, Y)}{\sigma_{X_i} \sigma_Y} \quad (2.3)$$

The PCC ranges from -1 to 1 , with values near -1 indicating a strong negative linear relationship, near 1 indicating a strong positive linear relationship, and values near 0 suggesting no linear correlation. While the PCC is a powerful metric for linear models, its reliance on the assumption of normality and sensitivity to outliers can limit its applicability, especially in scenarios involving non-linear or noisy data.

The Spearman Rank Correlation Coefficient (SRCC) is a non-parametric alternative that evaluates monotonic relationships by ranking the data values. It is given in Equation (2.4) where d_i is the difference between the ranks of X_i and Y for each observation, and n is the number of data points.

$$\rho_s = 1 - \frac{6 \sum d_i^2}{n(n^2 - 1)} \quad (2.4)$$

Unlike PCC, SRCC does not assume a specific distribution for the data and is robust against outliers, making it particularly suitable for non-linear dependencies or data with irregular distributions. By focusing on rank rather than magnitude, it captures the direction and consistency of relationships, rather than their specific form. Both PCC and SRCC are often used in preliminary SA to identify influential parameters and prioritize further exploration.

2.4.2 Morris Method

The Morris method is a GSA technique designed for computational efficiency in screening the impact of input parameters on model outputs (Morris 1991; Campolongo et al. 2011). It evaluates the elementary effects (EE) of each parameter by perturbing one parameter at a time while keeping the others fixed, thus estimating the local sensitivity across the input space. The elementary effect for a parameter X_i is calculated as in Equation (2.5) where f represents the model, Δ is the step size, and X_1, \dots, X_k are the model inputs.

$$EE_i = \frac{f(X_1, \dots, X_i + \Delta, \dots, X_k) - f(X_1, \dots, X_i, \dots, X_k)}{\Delta} \quad (2.5)$$

The method involves multiple random samplings of the input space, ensuring a broad representation of the parameter's effect across different regions. Two key metrics are derived from the EE: the mean of the absolute values of EE (μ^*), which reflects the overall influence of a parameter on the output, and the standard deviation (σ), which captures non-linear effects and interactions.

The mean of absolute effects is computed in Equation (2.6) where r is the number of sampled trajectories, and $|EE_{ij}|$ represents the absolute elementary effect for the j -th trajectory.

The standard deviation is given in Equation (2.7).

$$\mu^* = \frac{1}{r} \sum_{j=1}^r |E E_{ij}| \quad (2.6)$$

$$\sigma = \sqrt{\frac{1}{r-1} \sum_{j=1}^r (E E_{ij} - \mu)^2} \quad (2.7)$$

A high μ^* indicates a parameter with significant overall influence, while a high σ suggests interactions or non-linear dependencies with other parameters. The Morris method is well-suited for high-dimensional models, where variance-based SA is impractical. However, its approximation of interaction effects limits its use for detailed analysis, making it more appropriate for initial parameter screening and prioritization.

2.4.3 Sobol Indices

The Sobol method is a variance-based GSA technique that decomposes the output variance of a model into contributions from individual input parameters and their interactions (Sobol' 1990; Sobol 2001). This decomposition allows for a quantification of how much each parameter or combination of parameters influences the variability in the output. The total variance of the model output Y is expressed in Equation (2.8) where V_i is the variance contribution from parameter X_i , V_{ij} is the variance due to the interaction between X_i and X_j , and higher-order terms represent interactions among more parameters.

$$\text{Var}(Y) = \sum_{i=1}^k V_i + \sum_{i < j} V_{ij} + \dots + V_{1,2,\dots,k} \quad (2.8)$$

Using this decomposition, Sobol indices are defined to measure the relative contribution of each parameter or group of parameters to the total variance.

The first-order Sobol index quantifies the direct contribution of a single parameter X_i to the variance and is given by Equation (2.9).

$$S_i = \frac{V_i}{\text{Var}(Y)} \quad (2.9)$$

This index indicates how much of the output variance can be attributed solely to X_i . The total-order Sobol index accounts for both the direct and interaction effects involving X_i and is

calculated as in Equation (2.10) where $\text{Var}(Y|X_i)$ is the variance of Y when X_i is fixed, representing the residual variance from all other parameters.

$$S_{Ti} = 1 - \frac{\text{Var}(Y|X_i)}{\text{Var}(Y)} \quad (2.10)$$

Sobol indices are typically estimated using Monte Carlo or quasi-Monte Carlo sampling, requiring multiple evaluations of the model. While computationally intensive, the Sobol method is particularly valuable for understanding complex, non-linear models with significant interactions among parameters. Its ability to fully decompose variance makes it a cornerstone of SA for detailed exploration of model behavior.

2.5 Machine Learning for Validation

Machine learning is a subset of artificial intelligence that enables computational systems to learn from data and make predictions or decisions without being explicitly programmed (Baker et al. 2019). Unlike traditional algorithms that rely on predefined rules and structured logic, machine learning models employ statistical techniques and optimization strategies to iteratively refine their performance based on experience. This adaptability allows them to handle complex and dynamic datasets for predictive maintenance and scientific computing.

Among the most fundamental structures in deep learning are artificial neural networks (ANNs), which are computational models inspired by the neural architecture of the human brain (Yegnanarayana 2009). These networks consist of layers of interconnected artificial neurons, each performing mathematical transformations on input data. The core components of an ANN include an input layer that receives numerical representations of features, one or more hidden layers that process and transform the data, and an output layer that generates the final prediction or classification. Learning in ANNs occurs through the adjustment of connection weights between neurons, a process optimized using techniques like gradient descent and backpropagation. Activation functions such as the rectified linear unit (ReLU), sigmoid, and hyperbolic tangent introduce non-linearity into the model, allowing it to capture complex patterns and relationships (Sharma et al. 2017). The architectural flexibility of ANNs enables their application in diverse domains, from autonomous systems and medical diagnostics to real-time monitoring of industrial processes. A visualization of a simple feedforward ANN is presented in Figure 2.8, illustrating the flow of information from input features through multiple hidden layers before reaching the output layer.

The design of ANNs can be specialized based on the nature of the data and the problem

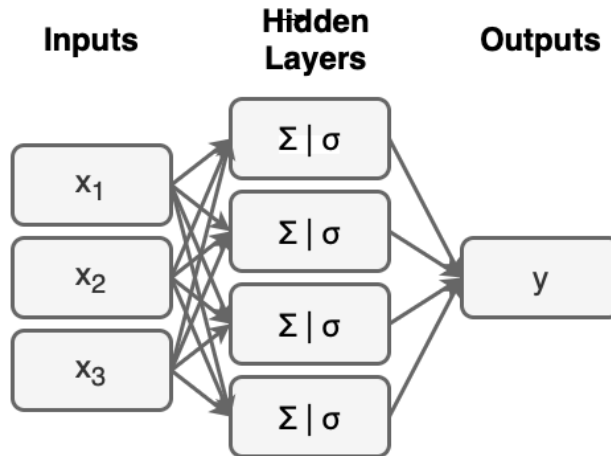


Figure 2.8: Outline of a one-layer neural network with a representation of the activation function to obtain the outputs.

being addressed. Recurrent neural networks (RNNs) are particularly well-suited for handling time-dependent data, as they maintain internal memory that allows them to process sequences efficiently, making them ideal for applications such as speech recognition, language modeling, and time-series forecasting (Medsker et al. 2001). However, traditional RNNs struggle with learning long-term dependencies due to the vanishing gradient problem, which is addressed by long short-term memory (LSTM) networks through specialized gating mechanisms that enable the retention of information over extended time intervals. LSTMs selectively update, forget, and output information, making them widely used for modeling complex temporal patterns in sensor validation, anomaly detection, and forecasting applications. Extending these capabilities, autoencoders provide a framework for learning efficient representations of data in an unsupervised manner, consisting of an encoder that compresses input into a lower-dimensional latent space and a decoder that reconstructs the original input. When combined with LSTMs, autoencoders become powerful tools for reconstructing missing sensor data, detecting anomalies, and validating measurements by learning expected outputs from historical data and identifying deviations that may indicate sensor faults or system anomalies.

2.5.1 Autoencoders

Autoencoders are a class of ANNs designed for learning efficient representations of input data, often applied to tasks such as dimensionality reduction, anomaly detection, and feature extraction (Lange and Riedmiller 2010; Wang et al. 2014). Unlike traditional ANNs that are trained for classification or regression, autoencoders focus on reconstructing their input data by encoding it into a compressed latent representation and then decoding it back to its original

form. This structure comprises two main components: the encoder, which maps the input data to a lower-dimensional space, and the decoder, which reconstructs the input from the compressed representation. The objective of an autoencoder is to minimize the reconstruction error, ensuring that the essential characteristics of the data are retained while reducing noise and redundancy. Figure 2.9 presents a schematic of an autoencoder, demonstrating how data is transformed through successive layers to create a compact yet informative representation before being reconstructed by the decoder.

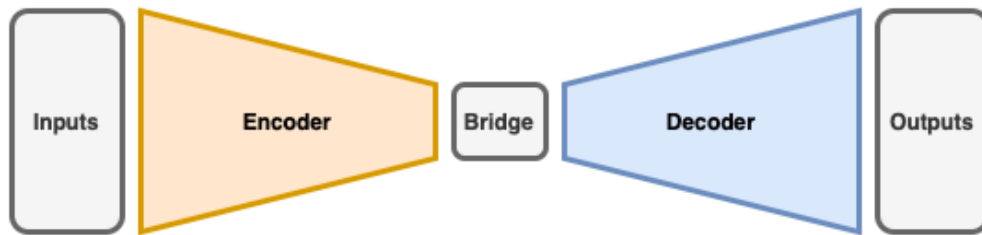


Figure 2.9: Simple diagram of an autoencoder showing the compression of inputs and decoding to obtain the outputs.

2.5.2 LSTM Networks

LSTM networks are a specialized form of RNNs designed to address the limitations of traditional RNNs in learning long-range dependencies (Graves and Graves 2012). Standard RNNs suffer from the vanishing gradient problem, which causes difficulty in retaining information across extended sequences (Noh 2021). LSTMs overcome this challenge by incorporating memory cells that selectively retain, update, or discard information through three gating mechanisms: the input gate, forget gate, and output gate. The input gate determines how much new information should be incorporated into the memory cell, the forget gate decides which portions of the stored information should be discarded, and the output gate regulates how much of the memory state should contribute to the final output. This structure allows LSTMs to effectively capture long-term dependencies in sequential data, making them particularly valuable in applications such as speech recognition, machine translation, and financial time-series forecasting. Figure 2.10 provides a visualization of an LSTM cell, illustrating how information is dynamically processed through its gating mechanisms.

In this study LSTM-based autoencoders are used in the validation of DFOS, which are used for high-resolution temperature monitoring in high temperature environments. These sensors provide valuable data for assessing thermal conditions in critical systems such as

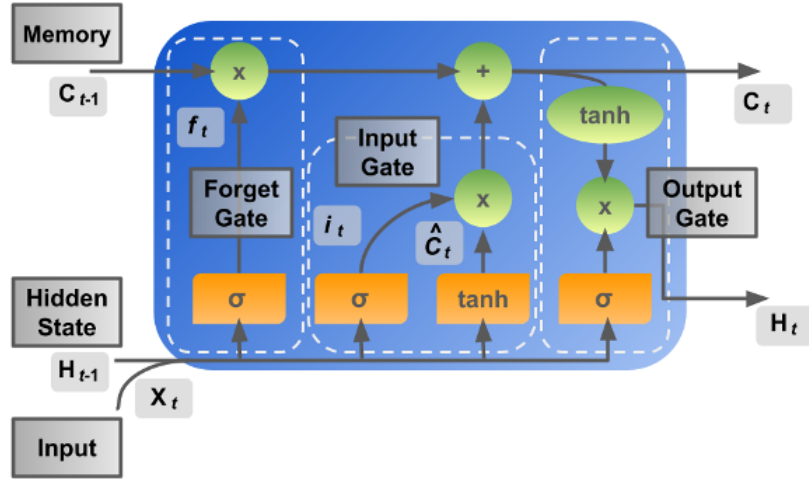


Figure 2.10: A diagram of a LSTM memory cell with its key gating mechanisms.

nuclear reactors, aerospace components, and industrial heat exchangers. Figure 2.11 illustrates an LSTM autoencoder applied to temperature monitoring data from a thermal hydraulic experiment, where input from thermocouples and fiber optic sensors is processed to validate sensor readings. The model learns to reconstruct expected temperature profiles and detect deviations.

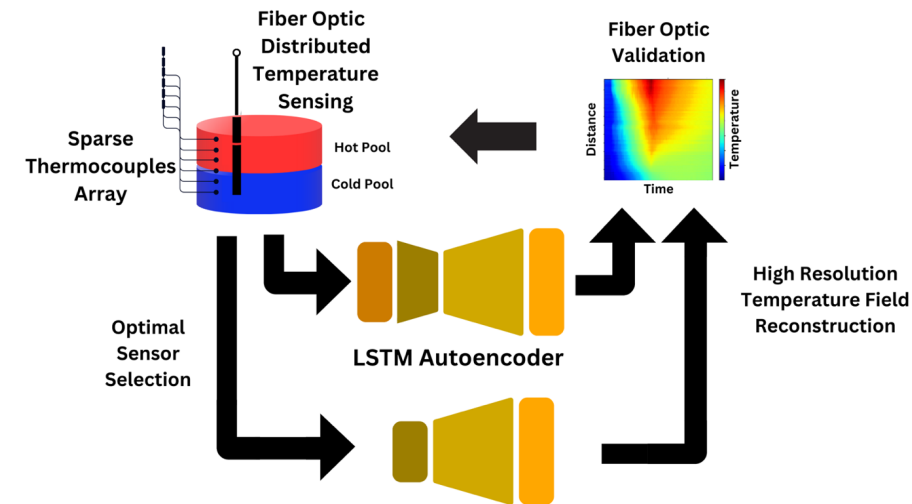


Figure 2.11: Layout of the LSTM autoencoder for validation of DFOS using input from thermocouples.

CHAPTER

3

CASE STUDY 1: WATER MIXING TEE RESULTS

In this chapter, results obtained from the water mixing tee located at Argonne National Laboratory are displayed. The methodology for obtaining this data is written in Section 2.2.1. A piping loop containing water as the coolant circulates in a counter-clockwise manner. The water is split to heat some of the coolant, where it is then mixed with the bulk of the flow. Temperature measurements are taken as a function of time across a few different transients through operating the pump at different speeds.

This chapter will describe in more detail how fiber optics measure temperature through a systematic methodology that includes calibration, SA of each measurement location, and validation using a machine learning model. The Bayesian calibration approach applied here builds upon prior work on distributed fiber optic temperature sensing, as detailed in (Kohler et al. 2024d,e), which introduced an advanced uncertainty quantification framework using DRAM for parameter estimation. By leveraging Bayesian inference, the methodology refines the conversion of Rayleigh scattering-based frequency shifts to temperature readings, thereby reducing measurement uncertainties and improving reliability.

Additionally, the SA techniques employed in this study are informed by the findings in (Kohler et al. 2024a), where GSA metrics, including Morris screening and Sobol' indices, were

used to rank the influence of different sensing locations on the overall system accuracy. This SA is critical for determining optimal calibration points and ensuring that fiber optic sensors provide high-fidelity measurements across the temperature field.

Furthermore, this chapter explores the integration of machine learning techniques for validating fiber optic temperature measurements. A LSTM autoencoder model is utilized to reconstruct distributed temperature profiles from sparse multi-point thermocouple arrays, complementing the Bayesian calibration and SA. This validation approach is particularly useful for detecting potential discrepancies between fiber optic sensors and traditional thermocouples. By incorporating these methodologies—Bayesian calibration, SA, and machine learning-based validation—this study enhances the accuracy and applicability of distributed fiber optic temperature sensing in thermal hydraulic systems.

3.1 Bayesian Calibration

The Rayleigh scattering fiber optic distribution sensors measure the frequency shift across the length of the fiber where the temperature can be obtained through a calibration curve. To perform calibration on the frequency shift calibration curve, the model must be defined as described in Equation 3.1 where T is defined as temperature in Celcius and S is the frequency shift in GHz based on previous relations (Weathered et al. 2017).

$$T = a|S|^b + c \quad (3.1)$$

To make more inferences about the parameters within the model of the calibration curve, MCMC DRAM is employed to better approximate the estimates of the parameters along with the uncertainties. The parameters are initialized as $\theta = [\theta_1 = a, \theta_2 = b, \theta_3 = c]$ where these values can be found from previous relationships by Weathered (Weathered et al. 2017) and set to be as follows: $\theta = [\theta_1 = 1.569, \theta_2 = 0.855, \theta_3 = 22.4]$. In the definition of DRAM for the parameters, sampling can be limited within range to better model the distribution. In this case, the parameters a and c are constrained in the positive domain or $(0, +\infty)$ based on physical phenomena and b is limited between $(0, 1)$ to lead to a faster convergence and a more realistic fit of the model. For calibration purposes, the fiber optics sensors are co-located at the same spatial axial position with four other thermocouples. The function optimized through MCMC DRAM is root mean square error where the inputs are the fiber optic frequency measurements and the output is obtained of the temperature measurements from the co-located thermocouple measurements. A total of 100,000 samples are modeled as benchmarking shows convergence at this amount of samples.

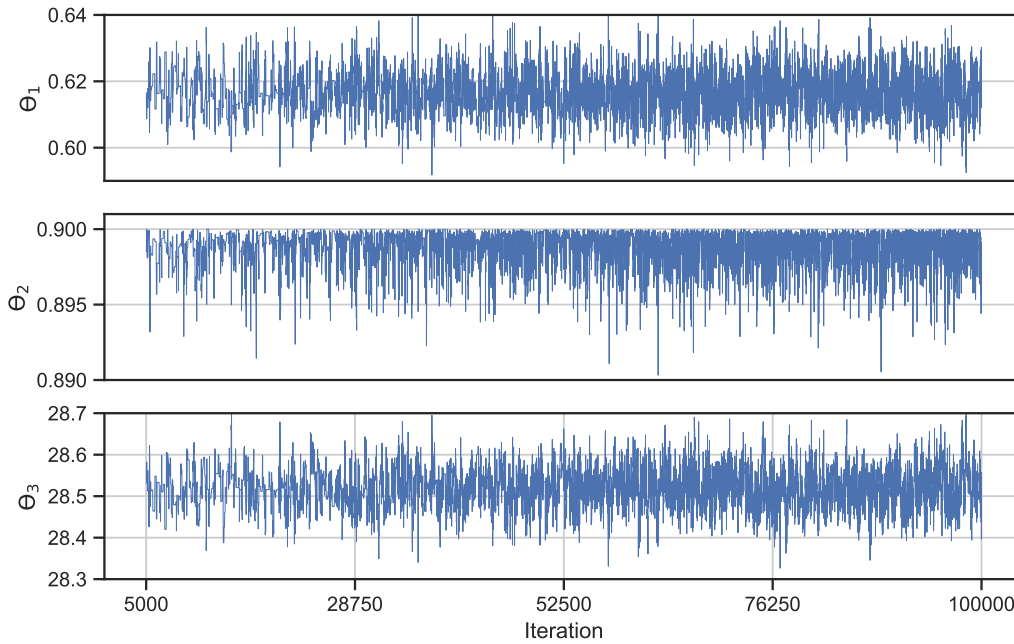


Figure 3.1: Chain plots obtained after 100,000 samples using DRAM with a 5,000 burn-in to approach convergence for the distribution.

As shown in Figure 3.1, the sample chains are shown where they appear to well explore the data. A burn-in time is applied at 5,000 samples as initially it takes time for the model to determine where the parameters are distributed around. To further show convergence of the chains, the ACF plots are shown in Figure 3.2 where each of the parameters converges to around 0 after about 30 lags, implying that every 30 samples is approximately independent of the following sample. Applying statistical estimators of the expected value and uncertainty based on the burn-in time and ACF findings by limiting to every 30th sample, Table 3.1 is able to obtain the posterior distribution of the fitted calibration parameters. To further evaluate the distribution of the samples obtained from MCMC DRAM, a distribution plot is shown in Figure 3.3 along the main diagonal. Furthermore, the chain samples are plotted along the bottom triangle to represent any correlations among the samples where a negative correlation is shown between sample a and c along with well distribution between the others. A contour plot is also represented on the upper diagonal to better show the relationships between the parameters.

Figure 3.4 illustrates the residual error between the DFOS and the thermocouple array within the flow loop, comparing the prior and posterior parameter estimations. The prior errors, shown in blue, exhibit larger fluctuations and higher peak deviations, indicating greater discrepancies between the DFOS measurements and thermocouple readings before calibration.

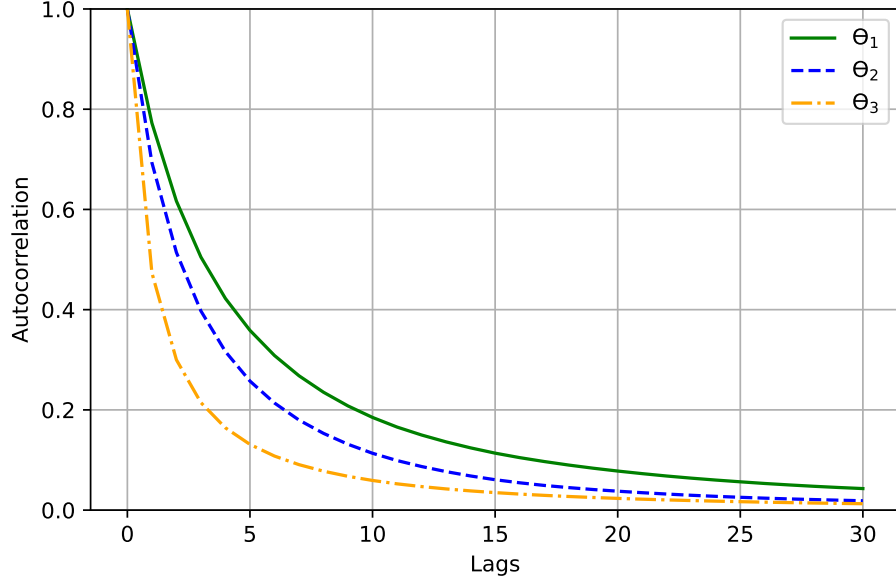


Figure 3.2: Auto-correlation plot as a function of lags to show the dependence of each sample proposition on the previous sample.

	Initial Values	Posterior Mean	Posterior STD	MC Error	Tau	Geweke
θ_1	1.569	0.62	6.09E-3	1.67E-4	98.95	1.00
θ_2	0.855	0.90	1.08E-3	2.72E-5	49.19	1.00
θ_3	22.40	28.52	0.05	1.25E-3	122.94	1.00

Table 3.1: Results obtained through sampling using DRAM to estimate the parameters with the initial values given alongside the posterior means, standard deviation, error with Monte Carlo sampling and other metrics.

After applying Bayesian inference with DRAM for parameter calibration, the posterior errors, shown in orange, demonstrate a noticeable reduction in variability and magnitude, suggesting improved agreement between the DFOS and thermocouple data. The reduction in residual error highlights the effectiveness of the DRAM calibration approach in refining the temperature conversion model and enhancing measurement accuracy. These improvements further validate the robustness of the Bayesian calibration methodology in minimizing systematic biases and uncertainties in DFOS-based temperature sensing.

3.2 Importance Ranking

In this case study, there are only 4 co-located axial locations of both the thermocouple and fiber optic sensors. Thus, reducing the total amount of thermocouples used to validate is trivial

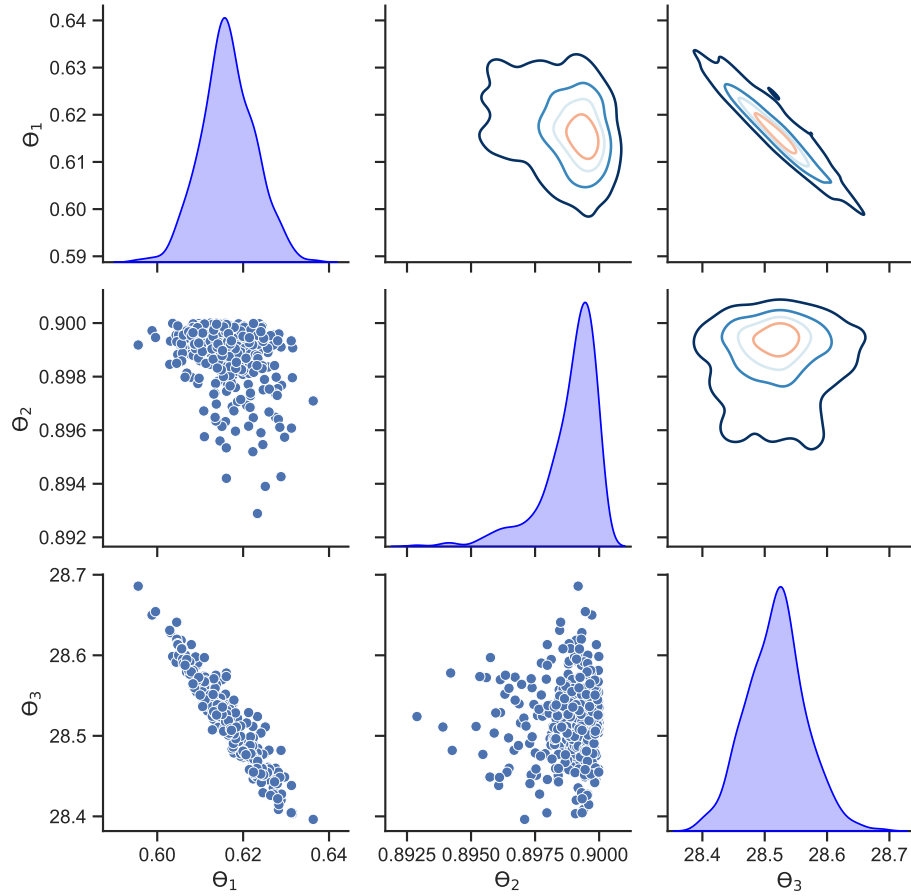


Figure 3.3: A distribution, correlation plot and contour plot of the parameter propositions as obtained through DRAM.

to reduce the thermocouple set. However, the SA is performed as a benchmark for the more intensive case as used in the following Chapter 4 when more co-locations are available.

Using the methodology of correlation coefficients, the Pearson and Spearman coefficients are determined as shown on a bar graph in Figure 3.5. The location of thermocouple 4 has the correlation for both the Pearson and Spearman indicating that it is most influential of a location for calibration. This is located at the top of the mixing loop after the cool and hot flow are well-mixed and turbulent flow is achieved.

Using another method of SA, Morris method is applied with results shown in Figure 3.6. Similar to the results shown from the correlation coefficients method, the location of the co-location of thermocouple 4 and the fiber optic is the most influential.

Lastly, a comprehensive approach is taken to apply Sobol indices to the measurements, as shown in Figure 3.7. The location of thermocouple 4 for first and total order indices is found to be the most influential, aligning with findings from correlation coefficients, where

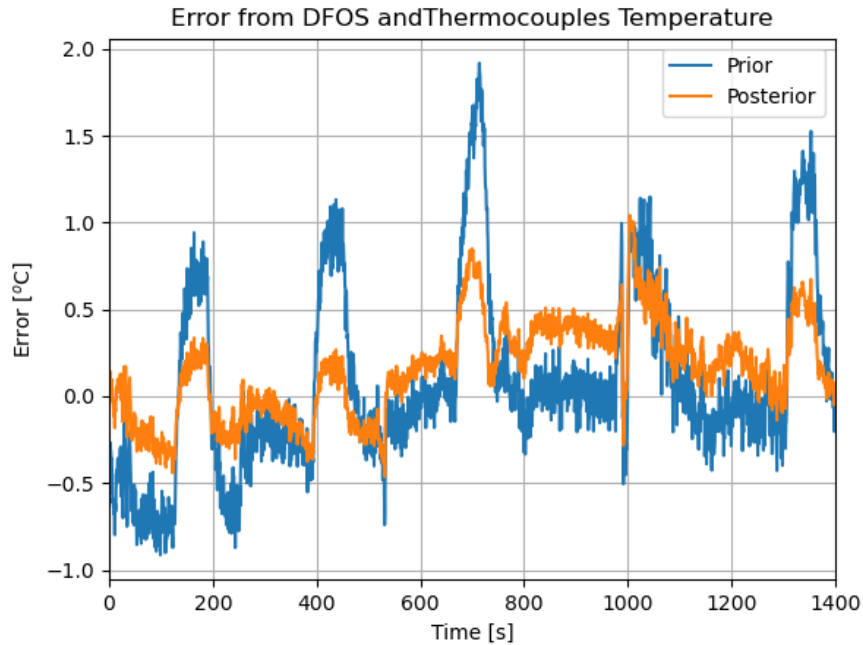


Figure 3.4: Residual error between the DFOS and thermocouple array within the flow loop comparing the prior parameters and the obtained parameters through DRAM for calibration of the parameters.

TC4 exhibited the strongest correlation with model output, surpassing the influence of TC1 and TC3, which demonstrated relatively lower correlations. Furthermore, second-order Sobol indices highlight a notable interaction effect between thermocouples 2 and 4, reinforcing the importance of TC4 in the temperature calibration process. This observation is consistent with the Morris method results, which indicate that TC4 not only has the largest mean absolute elementary effect but also the highest standard deviation, suggesting strong non-linearity and interaction effects. These findings collectively reinforce the significance of TC4 in the calibration and validation of temperature measurements, and the consistency of these results across multiple sensitivity analysis techniques—correlation coefficients, the Morris method, and Sobol indices—further validates the robustness of the assessment, confirming that the most critical locations for calibration are those positioned at a sufficient distance from the entry region, where the flow is fully developed.

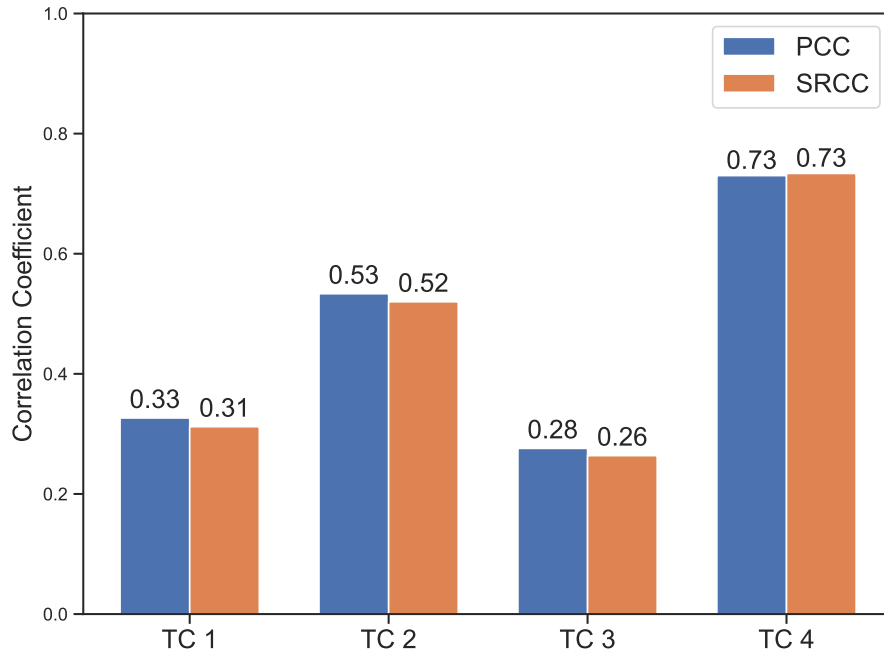


Figure 3.5: Pearson and Spearman correlation coefficients for each of the 4 co-located thermocouple sensors to determine the most important location for calibration purposes.

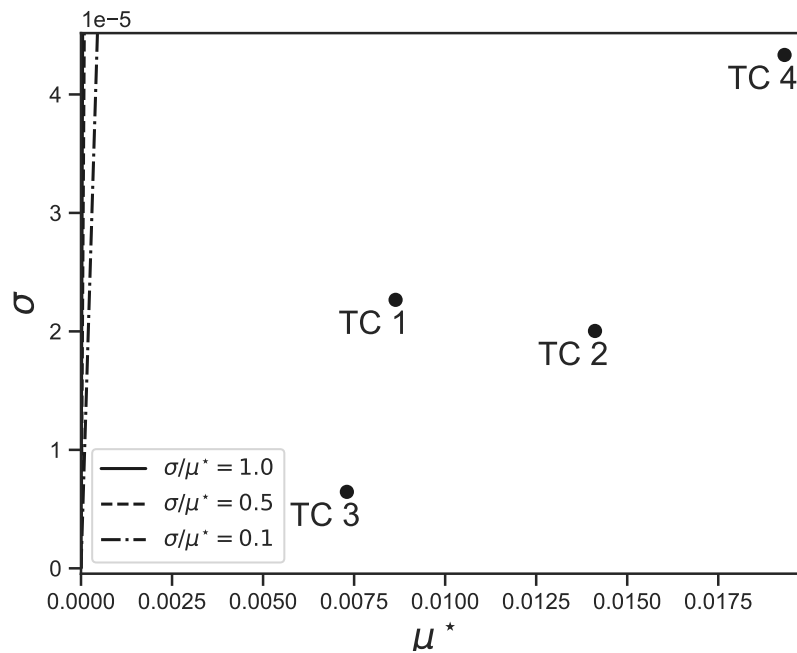


Figure 3.6: Results obtained of μ^* and σ from applying Morris method to the co-located temperature sensors within the mixing loop.

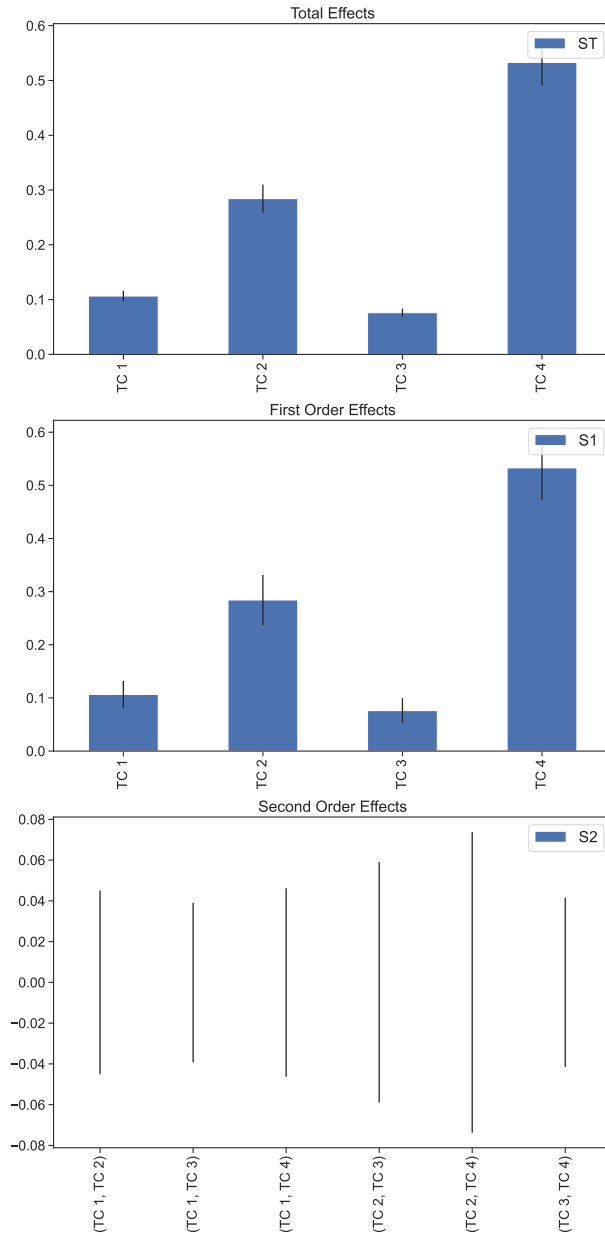


Figure 3.7: The total, first, and second order effects for the co-located temperature sensors within the flow loop.

3.3 Validation

A validation tool is implemented to establish a calibration device for DFOS. Using previous results, an LSTM autoencoder is employed to generate synthetic distributed fiber optic temperature measurements, which are compared against measured sensor data. The model is constructed with an input of four nodes corresponding to the thermocouple arrays used in

the measurements. This configuration is adaptable to accommodate different experimental setups and sensor distributions. The input data is compressed through a connected hidden layer to a dimensionality of one via the encoder, effectively reducing noise while preserving critical temperature patterns. After reaching the bridge, the data is expanded in the decoder to a dimensionality that matches the gage pitch of the DFOS, which operate on the millimeter scale, whereas thermocouples are spaced meters apart. This allows the model to infer detailed temperature distributions from a sparse sensor network, creating a higher-resolution representation of the temperature field.

The neural network training process begins with the dataset being divided into training, validation, and testing subsets. The first 50% of the data, corresponding to the first 700 seconds of the experiment, is designated as the training set. To ensure effective training, a validation set is used to monitor the process and detect potential overfitting. The mean square error is optimized throughout training, with an incremental RMSE vs. epoch plot shown in Figure 3.8 illustrating the model's learning progress. The RMSE curve shows a rapid decrease in early epochs, indicating efficient learning, followed by gradual stabilization, suggesting the model successfully converges to a reliable state. The validation set ensures that generalization is maintained, preventing the model from simply memorizing the training data.

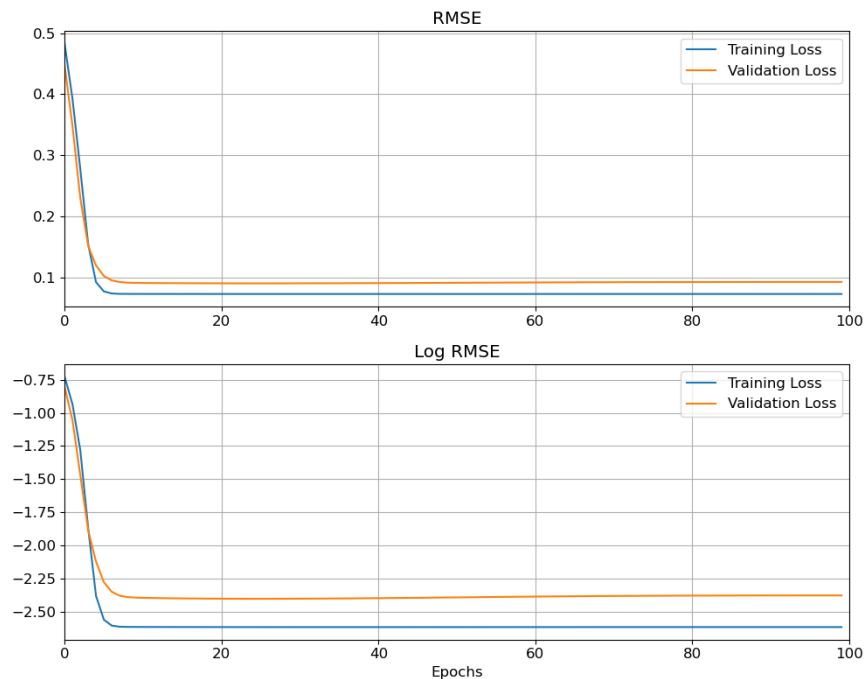


Figure 3.8: [Top] RMSE of the training of the LSTM autoencoder for validation of the DFOS through inputs of the thermocouples where the validation set and training set are denoted to show efficiency during training. [Bottom] Log RMSE plot to show more more minute changes.

Following the completion of training, additional analysis is conducted using the testing set, which consists of the final 600 seconds of measurement data. Thermocouple temperature readings serve as model inputs, predicting DFOS outputs. Residual errors for the predicted temperatures at each location are computed after processing through the LSTM autoencoder, as shown in Figure 3.9. The training data for TC 1 trends toward zero over time, demonstrating the effectiveness of LSTM neurons in capturing long-term dependencies. Similarly, TC 3 and TC 4 exhibit stable error reduction, trending toward zero. However, TC 2 deviates further from the measured value as time progresses, which is likely due to its position immediately before the mixing tee, where flow dynamics are less predictable, leading to increased temperature fluctuations and model uncertainty.

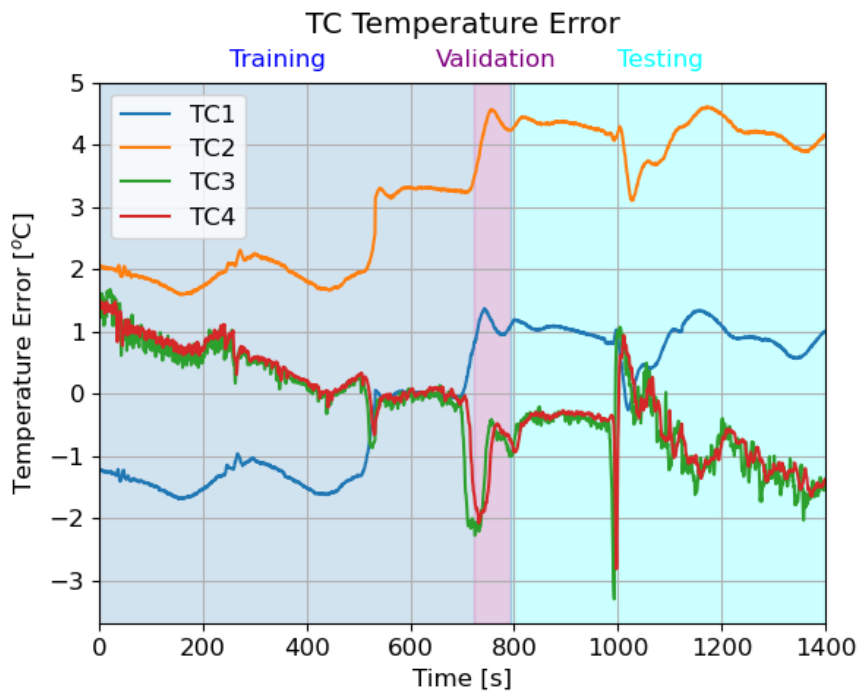


Figure 3.9: Residual error between the predicted temperature obtained from the LSTM autoencoder and measured thermocouple temperature from the flow loop. The training, validation, and testing set are shown over the test.

Additional comparisons are made between model predictions and fiber temperature measurements, as illustrated in Figure 3.10. With the exception of TC 1, the thermocouple arrays generally align with the measured values. TC 1 experienced issues during data collection, affecting the sensor’s overall reliability. The testing set reveals a similar pattern, with a noticeable spike of 1°C error occurring at the 1000-second mark, shown in Figure 3.9. This anomaly is likely

due to a transient event during the experiment, where a rapid temperature change occurred that was not well captured by the thermocouple inputs. However, the model adapts within approximately 75 seconds, correcting its predictions and maintaining accuracy.

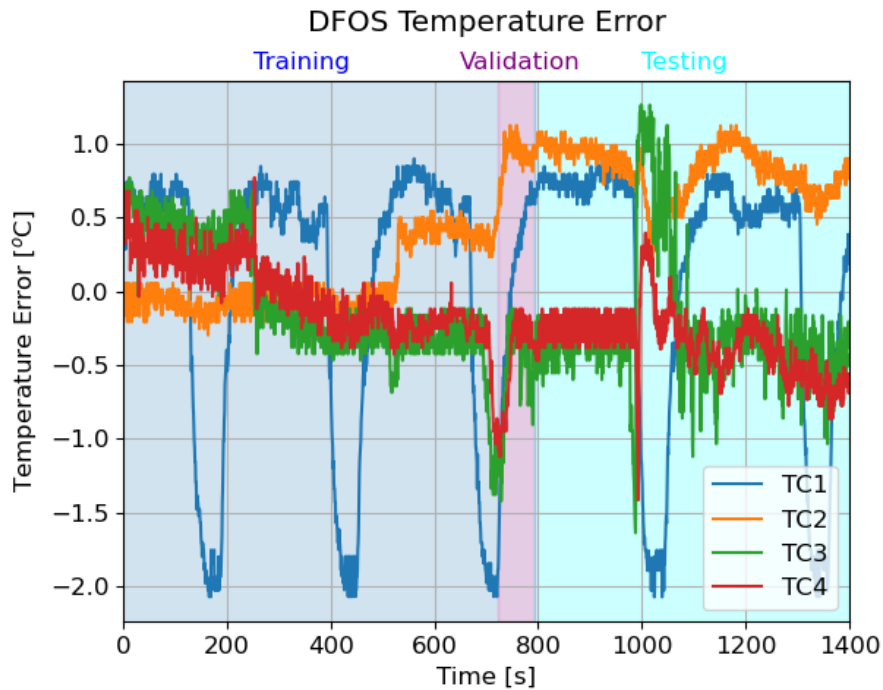


Figure 3.10: Error between the prediction found from the LSTM autoencoder and the temperature measurement from the distributed fiber optic temperature sensors.

Beyond this anomaly, the higher error observed in TC 2 remains consistent with previous results, reinforcing the influence of mixing flow conditions on sensor performance. This is further supported by Figure 2.2, where localized variations in temperature error align with regions of increased turbulence. The autoencoder’s ability to reconstruct high-resolution distributed temperature fields from sparse thermocouple inputs provides strong evidence that machine learning can be effectively applied to fiber optic sensor calibration. Future improvements could include expanding the input network to incorporate additional thermocouple measurements or integrating physical constraints to enhance model stability under transient conditions.

CHAPTER

4

CASE STUDY 2: LIQUID SODIUM THETA RESULTS

In this chapter, the methodologies developed are applied to the THETA to analyze distributed temperature sensing in a high-temperature sodium environment. THETA, a liquid sodium test facility at Argonne National Laboratory, is designed to investigate thermal stratification and natural circulation phenomena relevant to sodium-cooled fast reactors. Unlike the thermal mixing system, which utilizes a single co-located thermocouple/DFOS pair, THETA features three co-located thermocouple and fiber optic sensor locations distributed across the measurement plane. Each co-location contains 20 sensing points in the axial direction, significantly enhancing spatial resolution and enabling more comprehensive SA. This configuration allows for the identification of the most influential sensing locations, ultimately reducing the total number of points required for accurate temperature validation.

This chapter will detail the implementation of machine learning-based approaches, including an LSTM autoencoder for reconstructing temperature distributions from sparse multi-point thermocouple measurements, as previously demonstrated in (Kohler et al. 2023). By leveraging deep learning techniques, particularly LSTM networks, the model captures spatial and temporal dependencies within the temperature field, improving the accuracy of temperature prediction and validation in THETA. The use of these methods aligns with recent advancements

in multimodal learning for temperature reconstruction, where compression-based techniques have been explored to enhance sparse sensor data, as discussed in (Kohler et al. 2024b,c).

Through this application, the effectiveness of Bayesian inference for calibration and the integration of homogeneous transfer learning for sensor validation will be demonstrated. The results provide insights into temperature evolution within THETA during transient conditions, further supporting the deployment of advanced reactor monitoring techniques. This comprehensive approach enhances the reliability of distributed fiber optic temperature sensing, paving the way for improved reactor diagnostics and predictive modeling in liquid metal-cooled reactor systems.

4.1 Bayesian Calibration

In this section, the calibration of distributed fiber optic temperature sensors within the THETA facility is presented. Bayesian inference via the DRAM MCMC algorithm is utilized to establish the relationship between Rayleigh scattering frequency shifts and temperature. The initial parameters for the model, θ_1 , θ_2 , and θ_3 , are taken from prior correlation models and refined through Bayesian updates. The DRAM algorithm was run for 100,000 iterations, with a burn-in period of 5,000 samples to ensure the chain achieved a well spread. This burn-in period was determined based on the mixing observed in the trace plots of the samples, where parameter fluctuations stabilized and began to converge.

The trace plots for the calibration parameters, shown in Figure 4.1, demonstrate the stability of the DRAM sampling process after the initial burn-in period. These plots indicate sufficient mixing, with the chains effectively exploring the parameter space. The oscillations in the samples suggest that the algorithm has adequately captured the uncertainty in each parameter, ensuring that posterior estimates are reliable and reflective of the underlying system.

To better understand the relationships and independence between the calibration parameters, a pairwise scatterplot matrix of their posterior distributions is shown in figure 4.2. This matrix combines marginal distributions on the diagonal with off-diagonal pairwise scatterplots and density contours. The marginal distributions for θ_1 , θ_2 , and θ_3 reveal distinct shapes, indicating that each parameter's uncertainty has been effectively characterized. Notably, while θ_1 and θ_3 exhibit slight correlations, the remaining pairs of parameters appear largely uncorrelated. The density contours and scatterplots confirm that the sampling has explored the parameter space comprehensively, avoiding narrow or overly restrictive regions.

Autocorrelation plots, shown in figure 4.3 further validate the performance of the DRAM algorithm. These plots display the autocorrelation of the samples for each parameter as a function of lag, showing how quickly successive samples become independent. For all three

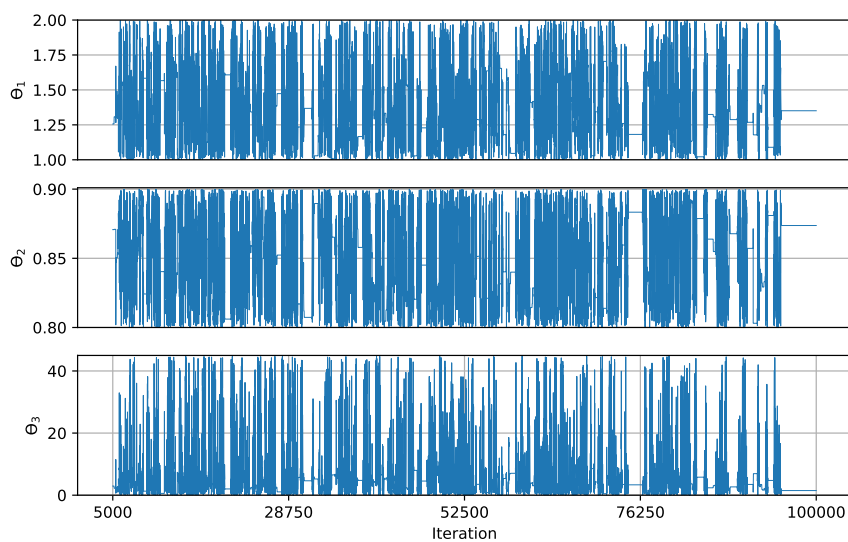


Figure 4.1: Chain samples obtained through DRAM methodology from data in THETA.

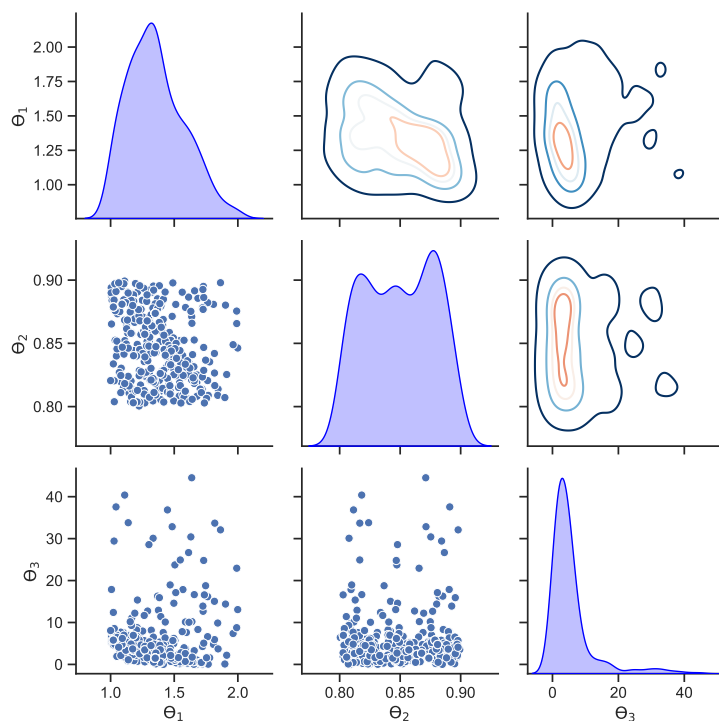


Figure 4.2: Distribution from the samples obtained through DRAM with more detail shown in pair plots in the bottom diagonal and contour plot shown in the upper diagonal.

parameters, autocorrelation decays rapidly within the first 30 lags, demonstrating the efficiency

of the sampling process and the minimal dependency between samples. This efficiency ensures that the effective sample size is sufficiently large, allowing for robust parameter estimation and uncertainty quantification.

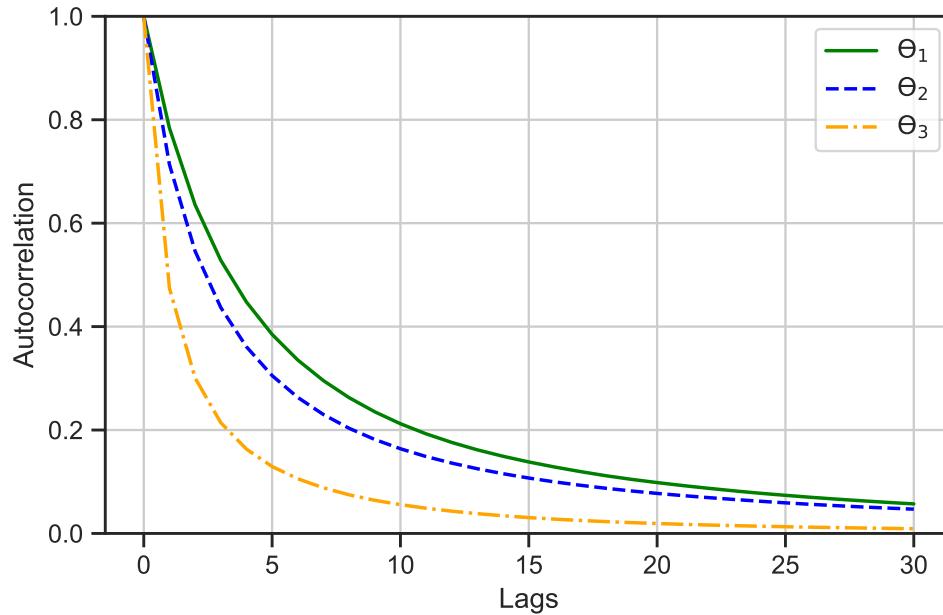


Figure 4.3: Autocorrelation plot of the estimated parameters in the calibration curve of the distributed fiber optic sensors in THETA.

The calibration methodology effectively reduces discrepancies between the modeled and measured temperature values, with detailed findings summarized in Table 4.1. This table includes posterior means, standard deviations, and other diagnostic statistics such as Monte Carlo error and Geweke convergence scores, confirming the reliability of the calibration process. By employing the DRAM approach, the calibration achieves improved accuracy in the conversion of Rayleigh scattering signals to temperature values, providing a solid foundation for SA and further refinement of the system. The use of 100,000 samples with a burn-in of 5,000 ensures that the posterior distributions are well-characterized, supporting the robust deployment of DFOS in the THETA facility.

	Initial Values	Posterior Mean	Posterior STD	MC Error	Tau	Geweke
θ_1	1.569	0.856	2.22E-4	1.38E-5	3.169	1.00
θ_2	0.855	0.802	2.20E-5	2.76E-6	25.20	1.00
θ_3	22.40	27.25	0.179	2.62E-2	139.4	1.00

Table 4.1: Parameter estimates derived from DRAM sampling, comparing initial values with posterior means, standard deviations, Monte Carlo sampling error, and additional statistical metrics.

4.2 Importance Ranking

Sensitivity analysis was conducted to identify the most critical thermocouple locations and optimize sensor placement for future applications. The analysis utilized cumulative explained variance, PCC, SRCC, the Morris method, and Sobol indices to evaluate the importance of each thermocouple.

Figure 4.4 presents the cumulative explained variance for the thermocouple array, providing a comprehensive view of the contribution of thermocouples to the overall variance. The plot indicates that the variance captured by the thermocouple array increases rapidly with the first few sensors, with two to three thermocouples capturing approximately 98% of the variance. Beyond this point, the curve flattens significantly, indicating diminishing returns for additional sensors. This finding suggests that only a few strategically placed thermocouples are necessary for accurate validation, reducing the need for a dense sensor array and enabling a more streamlined setup. These results not only improve the efficiency of sensor placement but also provide insight into the most information-rich locations within the system.

Figure 4.5 shows the PCC and SRCC values for each thermocouple, which assess the sensitivity of each location to flow dynamics. The thermocouples at lower indices exhibit the highest correlation coefficients for both PCC and SRCC, emphasizing their importance in capturing reliable and representative flow behavior. These regions, typically located closer to the inlet, are characterized by more stable temperature gradients and less turbulent flow, resulting in higher certainty in measurements. The gradual decline in correlation coefficients with increasing thermocouple index reflects the reduced sensitivity in regions with greater turbulence and thermal mixing. The consistent agreement between PCC and SRCC across all thermocouples reinforces the reliability of these findings and underscores the robustness of these metrics in assessing sensor importance.

Figure 4.6 illustrates the Morris method results, highlighting the mean absolute effect (μ^*) and its associated variability for each thermocouple. This method provides a quantitative measure of each sensor's influence on the model. Thermocouples at lower indices consistently show

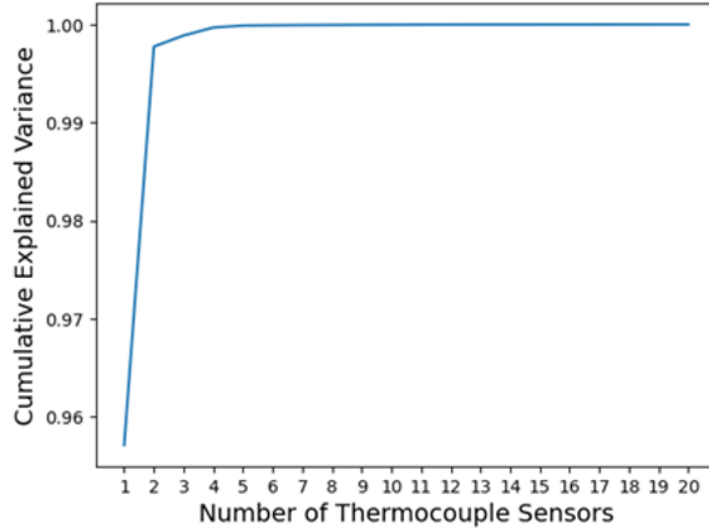


Figure 4.4: Cumulative explained variance of the thermocouple sensors necessary to have an accurate display of the axial range to reduce the total input size.

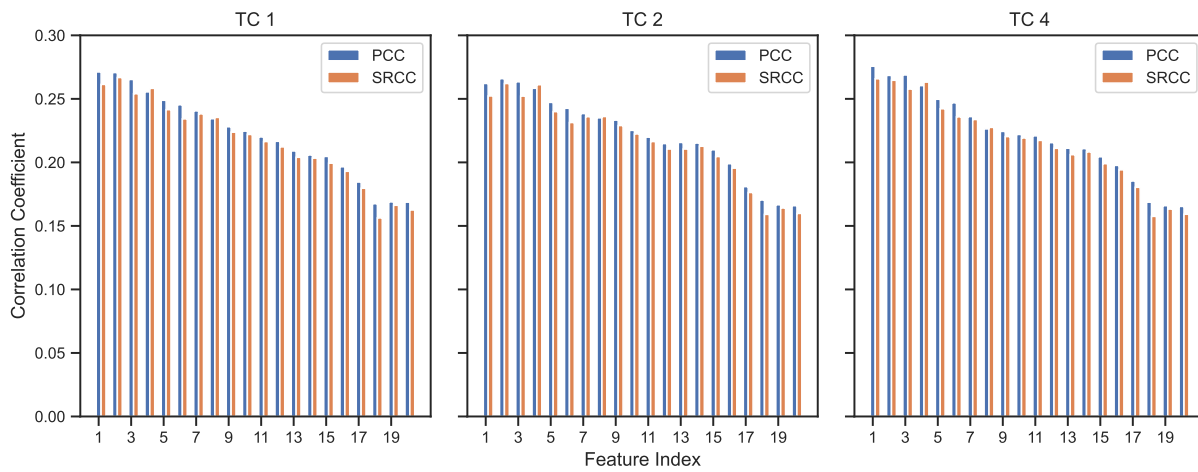


Figure 4.5: Pearson and Spearman correlation for each of the co-located sensors at 20 different axial locations.

the highest μ^* values, confirming their critical role in capturing essential flow characteristics. To enhance clarity, the standard deviation of the samples was scaled by a factor of 1,000, as the actual values were very small. This adjustment makes the variability more visually apparent and emphasizes the stability of the results. The declining μ^* values for thermocouples with higher indices further validate the reduced impact of these sensors on model accuracy. The combination of high μ^* values and low variability for the most critical sensors suggests that future sensor configurations can be optimized by focusing on these key locations.

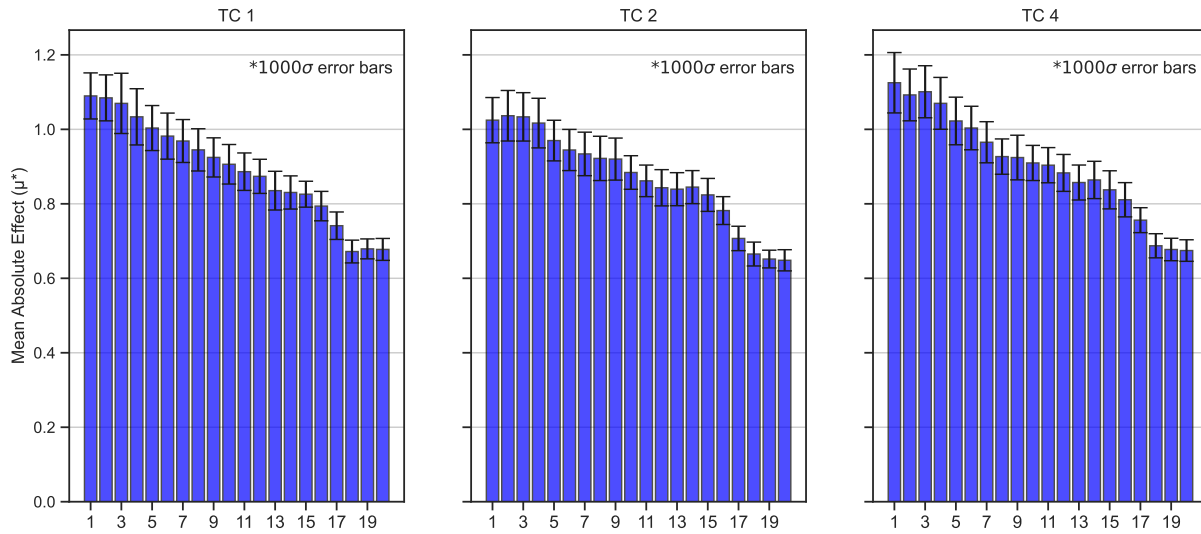


Figure 4.6: Morris method results at 3 different locations for the co-located sensors with each of the axial location denoted. Due to the low standard deviation of obtained from the method, a scale of 1000 is applied to show the magnitude.

The combination of these analyses highlights the potential to reduce the number of thermocouples required without compromising accuracy or reliability. By strategically selecting thermocouples based on their cumulative explained variance, correlation coefficients, and mean absolute effect, it is possible to achieve a cost-effective and efficient sensor configuration that maintains high data quality. The results from these SA provide a strategy for optimizing thermocouple placement. The clear patterns observed in the cumulative variance, correlation coefficients, and Morris method metrics show the value of focusing on a subset of thermocouples that provide the most significant information.

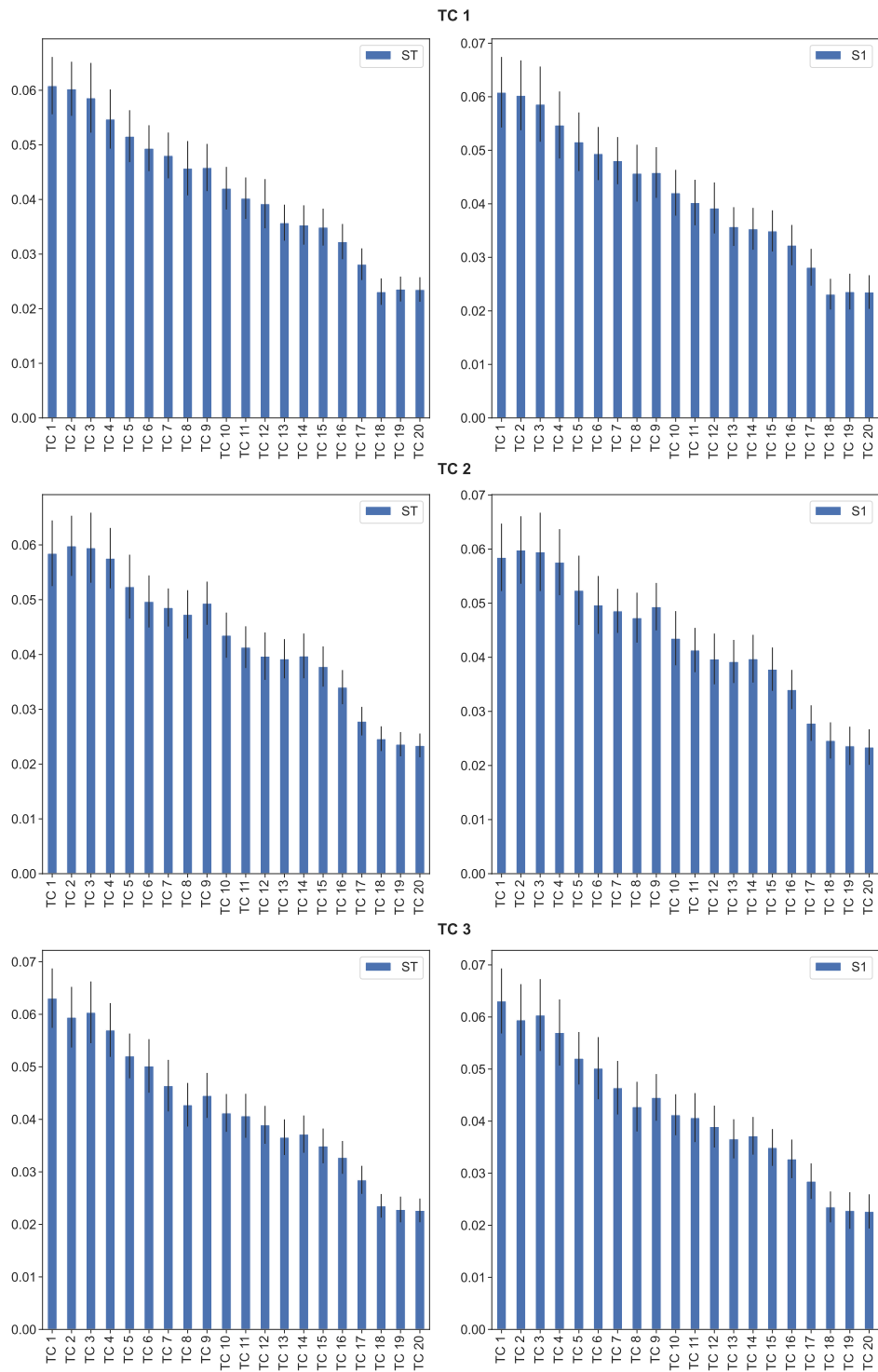


Figure 4.7: The first and total effects obtained from Sobol indices at the different locations for the co-located sensors.

4.3 Validation

To validate the system, an LSTM autoencoder was employed to predict temperature distributions based on input data from distributed thermocouple and fiber optic sensors. The model was trained using data from two out of the three co-locations, while the remaining co-location was reserved as the testing set to evaluate generalization. A 10% validation split was used during training to monitor performance and ensure the model did not overfit the training data. Results from the training are shown to converge towards a lower error over epochs as represented in Figure 4.8. The autoencoder was designed with an input size of 20, representing the thermocouples, and an output size of 520 to match the spatial resolution of the fiber optic sensors. It encodes the data into a latent space of size 2, capturing the critical variability identified by the cumulative explained variance plot, and then reconstructs the data back to the 520-point resolution to align with the fiber optics.

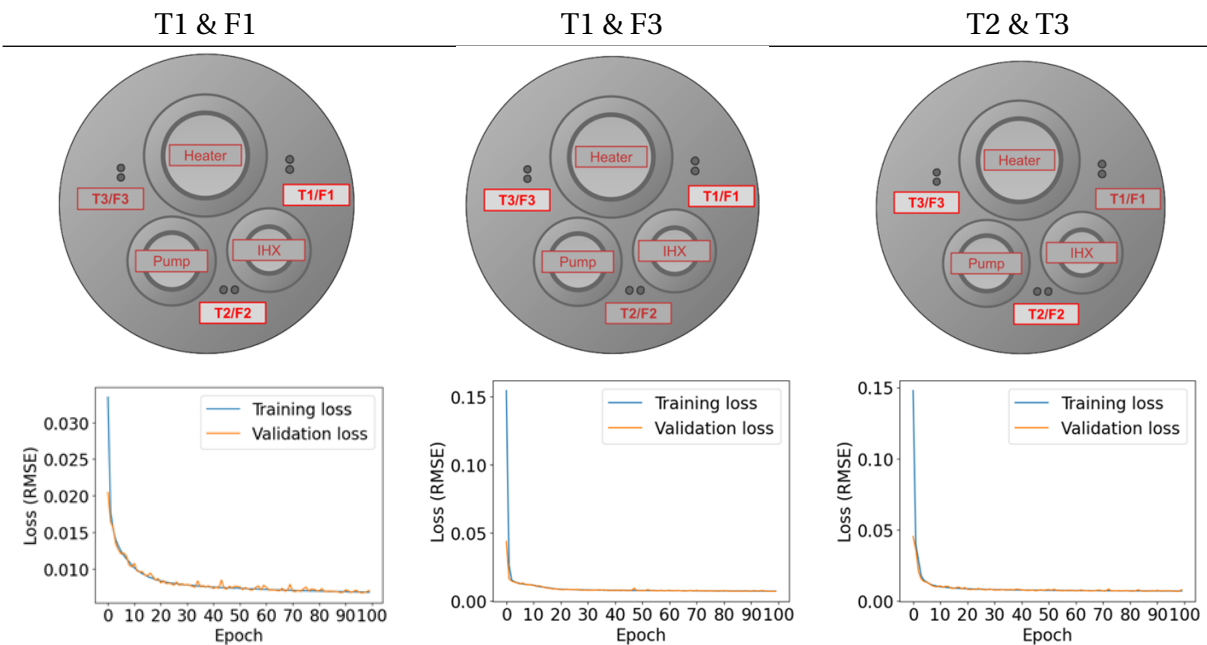


Figure 4.8: A detailed diagram showing results from the training loss with the validation loss also shown when training on 2 of the 3 co-located sensors.

The training setup and results are visualized in Figure 4.9, where the top row illustrates the experimental setup for each training scenario. Each configuration highlights the specific co-location pairs used for training, with the remaining co-location designated for testing. Below each schematic, the RMSE loss curves for both training and validation sets are plotted as

functions of epochs. These plots demonstrate a rapid decline in loss during the initial epochs, with both curves stabilizing at low values. This indicates that the model effectively learns the underlying patterns from the training data while avoiding overfitting. The consistently low validation loss across all scenarios reflects the model's ability to generalize well to unseen testing data.

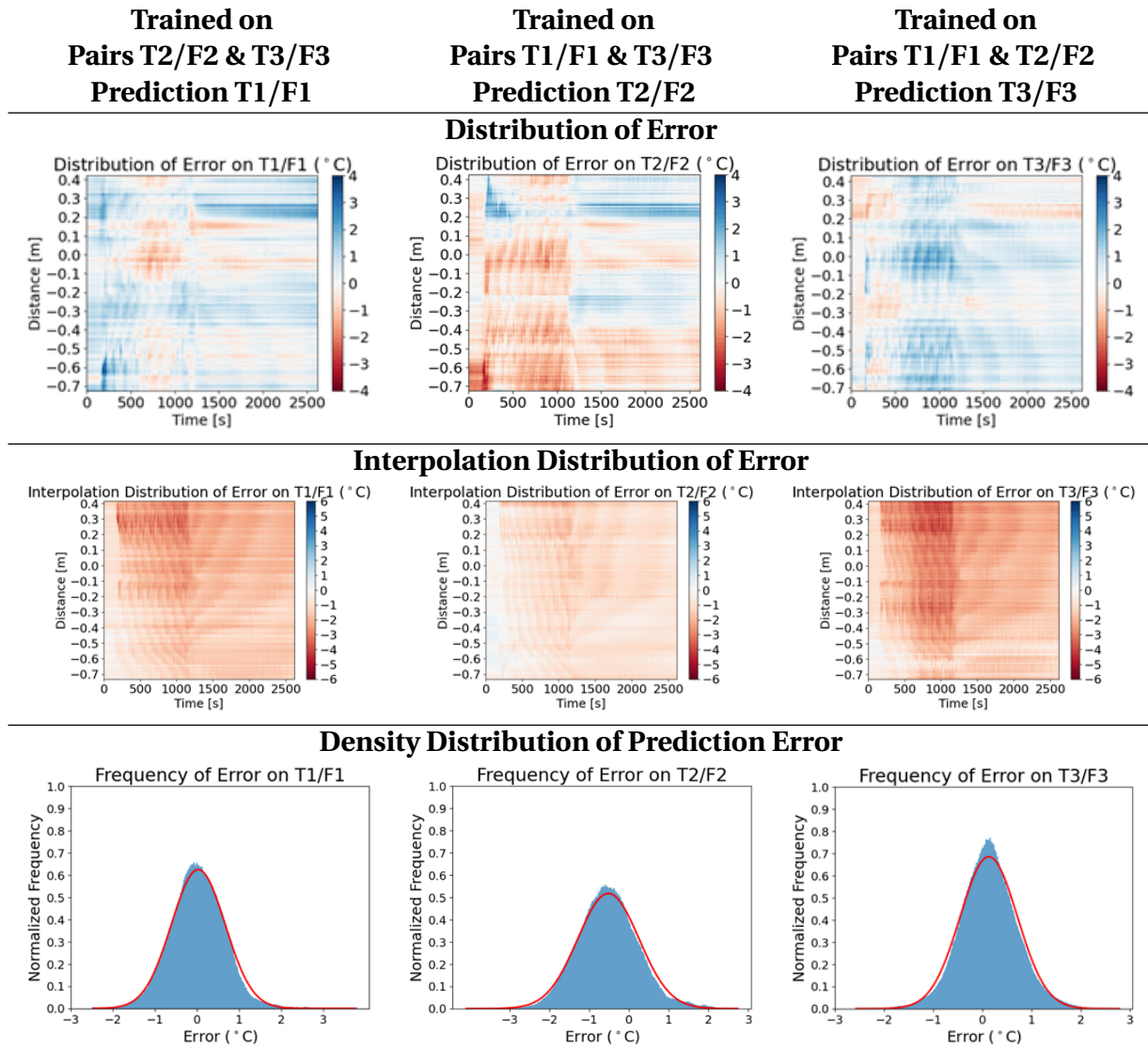


Figure 4.9: Comprehensive diagram of the error obtained when comparing the predicted temperature data and the measured DFOS. The top plots show the error over the 520 axial sensing location. A comparison is shown between predicting the temperature when using interpolation methods. A density distribution of the residual is shown in the bottom row of the figure.

The quantitative results of the training are summarized in Table 4.2, which lists the total training time and final RMSE values for each co-location pairing. All RMSE values are below 0.01°C, with minimal standard deviations, highlighting the model’s precision. For instance, the pairing of T1 and T3 achieves an RMSE of 0.00956°C with a standard deviation of 0.0139°C. While the training times vary slightly between configurations due to computational differences, they all remain efficient, with times ranging from approximately 944 to 1,302 seconds. These results confirm the autoencoder’s ability to efficiently and accurately map low-dimensional thermocouple data to high-resolution fiber optic outputs.

	T1 & T2	T1 & T3	T2 & T3
Training Time [s]	1052	944	1302
RMSE ± STD [°C]	0.00992 ± 0.0151	0.00956 ± 0.0139	0.00998 ± 0.0144

Table 4.2: The total training time on the LSTM autoencoder by running on an M1 Apple chip with the ending RMSE.

Further analysis of the model’s performance is provided in Table 4.3, which compares the prediction errors across co-locations for various training configurations. The results show consistently low errors for most setups. The errors are significantly lower than those produced by traditional interpolation methods, such as spline fitting, as seen in the final column. For example, training on T1/F1 and T3/F3 to predict T2/F2 achieves an error of $-0.00531 \pm 0.1845^\circ\text{C}$, which is an order of magnitude smaller than the corresponding spline error. This demonstrates the superiority of the LSTM autoencoder in handling complex, nonlinear relationships in the data.

The distribution of prediction errors is explored in Figure 4.9, which includes spatial-temporal heatmaps, interpolation distributions, and density plots of the errors. The spatial-temporal heatmaps show the error distributions for each co-location prediction over time and distance. These heatmaps reveal uniformly low errors across the tested regions, with no significant spatial or temporal bias. The interpolation distributions provide additional insight into the model’s accuracy when reconstructing data within the gaps between training locations. The density plots of prediction errors confirm a well-centered normal distribution with minimal spread, indicating high consistency and reliability in the model’s predictions.

Prediction	Error in LSTM Autoencoder [°C]			Spline Error [°C]
	Trained on T2/F2 & T3/F3	Trained on T1/F1 & T3/F3	Trained on T1/F1 & T2/F2	
T1/F1	0.02727 ± 0.6386	0.00064 ± 0.1932	-0.00662 ± 0.1930	1.89480 ± 0.6443
T2/F2	0.06133 ± 0.2179	-0.51993 ± 0.7712	-0.00531 ± 0.1845	1.01923 ± 0.4491
T3/F3	0.24188 ± 0.7922	0.00080 ± 0.2078	0.12794 ± 0.5822	1.65290 ± 0.8095

Table 4.3: Error metrics in °C for predictions using an LSTM Autoencoder trained on different data combinations, compared against spline interpolation errors. Spline interpolation errors are included as a reference for comparison.

Overall, the LSTM autoencoder demonstrates exceptional performance in reconstructing high-resolution temperature distributions from low-dimensional thermocouple data. By encoding critical variability into a compact latent space and efficiently reconstructing to fiber optic resolution, the model achieves high accuracy, efficient training, and generalization. The low RMSE values, minimal prediction errors, and consistent spatial-temporal accuracy highlight the autoencoder’s effectiveness as a tool for temperature profiling in complex systems. These findings validate the methodology and suggest significant potential for future applications where accurate, high-resolution data reconstruction is required.

CHAPTER

5

CONCLUSIONS

5.1 Summary of Results

The study investigated the application of Bayesian inference and sensitivity analysis for calibrating distributed fiber optic sensors (DFOS) in a high-temperature reactor environment, through the use of machine learning techniques to enhance predictive accuracy. By incorporating prior knowledge with experimental data, Bayesian inference significantly improved the accuracy of DFOS temperature readings, reducing the mean absolute error and strengthening the correlation between DFOS and reference thermocouples. The results showed that lower-temperature areas were the most indicative for accurate prediction locations, suggesting that temperature gradients play a crucial role in determining calibration accuracy. Residual differences between thermocouple and DFOS readings demonstrated that the largest improvements occurred in the lowest temperature segments, where prior temperature estimation errors were more pronounced.

Sensitivity analysis using Pearson and Spearman correlation coefficients confirmed a strong linear relationship between specific calibration parameters and temperature output, while Sobol' indices highlighted the most influential sensor locations contributing to measurement accuracy. The Morris screening method further identified key measurement locations that significantly affected overall model sensitivity. The experimental data demonstrated that the

thermocouple located downstream of the mixing zone had the highest sensitivity indices, emphasizing the importance of precise calibration in this region to ensure accurate model outputs. The calibration process utilized Bayesian inference through the Delayed Rejection Adaptive Metropolis (DRAM) algorithm, which efficiently refined the temperature conversion model. The posterior distribution obtained from experimental data indicated parameter values converging to optimal estimates, with the Bayesian calibration reducing uncertainty in parameter selection by over 50% compared to the initial prior estimates.

Additionally, a LSTM autoencoder was successfully trained to predict optical fiber temperature readings using co-located thermocouples. The model exhibited strong generalization capabilities, reducing prediction uncertainty while maintaining high spatial resolution. Performance metrics showed that the LSTM model achieved a maximum prediction error of $-0.51993 \pm 0.7712^\circ\text{C}$ compared with other methods, finding the smallest error at $1.01923 \pm 0.4491^\circ\text{C}$, confirming its reliability in reconstructing temperature profiles. The use of Principal Component Analysis (PCA) also determined the optimal number of thermocouples necessary for accurate temperature field reconstruction, demonstrating that over 99% of total variance could be retained using just three sensors strategically placed in high-impact regions.

From a computational standpoint, Bayesian calibration using the DRAM algorithm improved efficiency, converging faster with reduced computational time compared to traditional Monte Carlo methods. The MCMC chain analysis indicated rapid convergence with minimal autocorrelation, suggesting an efficient sampling process. The LSTM model required approximately 100 epochs for training, achieving a stable loss function with consistent predictions across different test cases. These results confirm the feasibility of using Bayesian inference, sensitivity analysis, and machine learning models for accurate and efficient validation of DFOS temperature measurements in advanced reactor systems, offering a robust framework for enhancing thermal-hydraulic monitoring and sensor reliability in high-temperature environments.

5.2 Conclusions

This study demonstrates the effectiveness of integrating Bayesian inference, sensitivity analysis, and machine learning techniques for the calibration and validation of distributed fiber optic sensors (DFOS) in high-temperature reactor environments. The results confirm that Bayesian calibration significantly enhances the accuracy of DFOS temperature measurements by incorporating prior knowledge and experimental data, reducing overall uncertainty in temperature predictions. Sensitivity analysis identified key locations along the optical fiber where calibration had the greatest impact, emphasizing that lower-temperature regions provided the most

reliable indicators for model refinement. The analysis further revealed that calibration parameters were most sensitive in areas experiencing significant thermal gradients, highlighting the importance of precise sensor placement and validation techniques.

The implementation of a Long Short-Term Memory (LSTM) autoencoder further validated the effectiveness of machine learning for reconstructing temperature profiles, reducing prediction errors and improving spatial resolution. The model's ability to generalize across varying conditions while maintaining a low mean absolute error underscores its potential for real-time monitoring applications in advanced reactor systems. Additionally, the Delayed Rejection Adaptive Metropolis (DRAM) algorithm efficiently refined calibration parameters, demonstrating improved convergence rates and computational efficiency over traditional Monte Carlo methods.

A key conclusion from this research is that a combination of physics-informed Bayesian inference and data-driven machine learning methods can substantially improve temperature monitoring in nuclear reactor environments. The findings suggest that future sensor calibration efforts should prioritize regions with high sensitivity to temperature variations and incorporate adaptive methodologies to refine parameter selection dynamically. The successful integration of these techniques provides a scalable and efficient framework for improving sensor accuracy, reducing operational uncertainty, and enhancing the reliability of temperature measurements in next-generation reactor systems.

5.3 Future Work

Building upon the advancements in Bayesian inference, machine learning, and uncertainty quantification demonstrated in this study, future research will explore new methodologies to further enhance the validation and calibration of distributed fiber optic sensors (DFOS) in high-temperature reactor environments. One promising direction is the application of different neural network architectures beyond the Long Short-Term Memory (LSTM) autoencoder used in this work. Investigating the use of Transformer-based models, convolutional neural networks (CNNs), and graph neural networks (GNNs) could provide improved spatial-temporal accuracy for reconstructing temperature fields. Transformers, in particular, have demonstrated strong performance in sequence modeling and could be leveraged to capture long-range dependencies in temperature variations. Hybrid models that combine CNNs for spatial feature extraction with LSTMs for temporal dynamics could also enhance prediction fidelity.

In addition to expanding machine learning techniques, future work will compare different Bayesian inference methods to assess their performance relative to the Delayed Rejection Adaptive Metropolis (DRAM) algorithm. Alternative Markov Chain Monte Carlo (MCMC) methods,

such as Hamiltonian Monte Carlo (HMC) and Sequential Monte Carlo (SMC), will be evaluated for their efficiency in calibrating DFOS data. HMC, which incorporates gradient information to improve sampling efficiency, may offer faster convergence compared to DRAM, particularly in high-dimensional parameter spaces. Variational inference (VI), an alternative to MCMC, could also be explored for its computational advantages in approximating posterior distributions with complex priors.

Uncertainty quantification (UQ) will be another critical focus, as improving confidence in temperature predictions is essential for practical reactor applications. Beyond Sobol' indices and Morris screening, future research will incorporate Gaussian process regression (GPR) for modeling uncertainty in temperature reconstructions. The use of Bayesian neural networks (BNNs) will be investigated as a means of propagating uncertainty through the machine learning model itself, providing probabilistic estimates of sensor validation accuracy. Additionally, information-theoretic approaches, such as mutual information-based UQ methods, could be employed to optimize sensor placement by maximizing the expected information gain from calibration experiments.

A particularly exciting avenue is the integration of reinforcement learning (RL) to enhance sensor calibration and validation. RL-based frameworks could dynamically adjust Bayesian inference models and machine learning algorithms based on real-time data acquisition, optimizing the calibration process adaptively. This approach could be particularly beneficial for automated reactor monitoring systems, where RL agents can learn optimal sampling strategies to reduce experimental uncertainty while minimizing computational costs. Combining RL with active learning techniques would enable an intelligent system that prioritizes the most informative sensor data, improving the overall efficiency of temperature field reconstruction.

Future experimental work will also expand validation efforts by incorporating additional reactor configurations and thermal-hydraulic conditions. Testing DFOS calibration methods under transient scenarios, including rapid heating and cooling cycles, will help evaluate the adaptability of Bayesian inference and machine learning techniques in dynamic environments. Further, applying these methodologies to more complex reactor geometries, such as liquid-metal-cooled fast reactors and molten salt reactors, will provide insights into their applicability for next-generation nuclear systems.

The ultimate goal of these future efforts is to develop a robust, adaptive framework that integrates Bayesian inference, deep learning, and reinforcement learning for real-time DFOS calibration and validation. By leveraging a diverse set of inference techniques and neural network architectures, these advancements will enhance sensor reliability, reduce operational uncertainty, and optimize temperature monitoring strategies for advanced nuclear reactors.

REFERENCES

- Abou-Jaoude, A., Lin, L., Bolisetti, C., Worsham, E. K., Larsen, L. M., and Epiney, A. S. (2023). Literature review of advanced reactor cost estimates.
- Akins, A., Kultgen, D., and Heifetz, A. (2023). Anomaly detection in liquid sodium cold trap operation with multisensory data fusion using long short-term memory autoencoder. *Energies*, 16(13).
- Alberti, A. L., Agarwal, V., Gutowska, I., Palmer, C. J., and de Oliveira, C. R. (2023). Automation levels for nuclear reactor operations: A revised perspective. *Progress in Nuclear Energy*, 157:104559.
- Ankel, V., Pantopoulou, S., Weathered, M., Lisowski, D., Cilliers, A., and Heifetz, A. (2020). One-step ahead prediction of thermal mixing tee sensors with long short term memory (lstm) neural networks. Technical report, Argonne National Lab.(ANL), Argonne, IL (United States).
- Ankel, V., Pantopoulou, S., Weathered, M., Lisowski, D., Cilliers, A., and Heifetz, A. (2021). Monitoring of thermal mixing tee sensors with lstm neural networks. *Proceedings of the 12th Nuclear Plant Instrumentation, Control and Human-Machine Interface Technologies (NPIC-HMIT2021), Providence, RI, USA*, pages 14–17.
- Aoto, K., Dufour, P., Hongyi, Y., Glatz, J. P., Kim, Y.-i., Ashurko, Y., Hill, R., and Uto, N. (2014). A summary of sodium-cooled fast reactor development. *Progress in Nuclear Energy*, 77:247–265.
- Arostegui, D. A. and Holt, M. (2019). Advanced nuclear reactors: technology overview and current issues. In *Congressional Research Service Report for Congress*. Library of Congress United States.
- Baker, N., Alexander, F., Bremer, T., Hagberg, A., Kevrekidis, Y., Najm, H., Parashar, M., Patra, A., Sethian, J., Wild, S., et al. (2019). Workshop report on basic research needs for scientific machine learning: Core technologies for artificial intelligence. Technical report, USDOE Office of Science (SC), Washington, DC (United States).
- Benoit, V. and Yappert, M. C. (1996). Effect of capillary properties on the sensitivity enhancement in capillary/fiber optical sensors. *Analytical chemistry*, 68(1):183–188.
- Campolongo, F., Saltelli, A., and Cariboni, J. (2011). From screening to quantitative sensitivity analysis. a unified approach. *Computer Physics Communications*, 182(4):978–988.
- Corkhill, C., Joyce, M., Lacey, D., and Thrift, N. (2025). Small and advanced nuclear reactors: Closing the fuel cycle? *Bulletin of the Atomic Scientists*, 81(1):43–47.
- Davydov, R., Antonov, V., Makeev, S., Batov, Y., Dudkin, V., and Myazin, N. (2019). New high-speed system for controlling the parameters of a nuclear reactor in a nuclear power plant. In *E3S Web of Conferences*, volume 140, page 02001. EDP Sciences.

- Ghafoori, Y., Vidmar, A., Říha, J., and Kryžanowski, A. (2020). A review of measurement calibration and interpretation for seepage monitoring by optical fiber distributed temperature sensors. *Sensors*, 20(19):5696.
- Girard, S., Alessi, A., Richard, N., Martin-Samos, L., De Michele, V., Giacomazzi, L., Agnello, S., Di Francesca, D., Morana, A., Winkler, B., et al. (2019). Overview of radiation induced point defects in silica-based optical fibers. *Reviews in Physics*, 4:100032.
- Graves, A. and Graves, A. (2012). Long short-term memory. *Supervised sequence labelling with recurrent neural networks*, pages 37–45.
- György, H. and Czifrus, S. (2015). Burnup calculation of the generation iv reactors. *Progress in Nuclear Energy*, 81:150–160.
- Haario, H., Laine, M., Mira, A., and Saksman, E. (2006). Dram: efficient adaptive mcmc. *Statistics and computing*, 16(4):339–354.
- Hashemian, H. and Jiang, J. (2009). Nuclear plant temperature instrumentation. *Nuclear Engineering and Design*, 239(12):3132–3141.
- Higdon, D., Gattiker, J., Williams, B., and Rightley, M. (2008). Computer model calibration using high-dimensional output. *Journal of the American Statistical Association*, 103(482):570–583.
- Huang, J., Blanquer, L. A., Gervillié, C., and Tarascon, J.-M. (2021). Distributed fiber optic sensing to assess in-live temperature imaging inside batteries: rayleigh and fbgs. *Journal of The Electrochemical Society*, 168(6):060520.
- Huang, M.-F., Salemi, M., Chen, Y., Zhao, J., Xia, T. J., Wellbrock, G. A., Huang, Y.-K., Milione, G., Ip, E., Ji, P., et al. (2019). First field trial of distributed fiber optical sensing and high-speed communication over an operational telecom network. *Journal of Lightwave Technology*, 38(1):75–81.
- Hyer, H. C., Giuliano, D. R., and Petrie, C. M. (2023). Toward local core outlet temperature monitoring in gas-cooled nuclear reactors using distributed fiber-optic temperature sensors. *Applied Thermal Engineering*, 230:120847.
- Hyvärinen, J., Vihavainen, J., Ylönen, M., and Valkonen, J. (2022). An overall safety concept for nuclear power plants. *Annals of Nuclear Energy*, 178:109353.
- Iooss, B. and Lemaître, P. (2015). A review on global sensitivity analysis methods. *Uncertainty management in simulation-optimization of complex systems: algorithms and applications*, pages 101–122.
- Jin, I. J. and Bang, I. C. (2024). The time for revolutionizing small modular reactors: Cost reduction strategies from innovations in operation and maintenance. *Progress in Nuclear Energy*, 174:105288.
- Kautzman, M., Jenkins, B., Joyce, P., and Brownell, C. (2018). Calibration and testing of distributed fiber optic sensors for detection of high energy radiation.

- Kennedy, M. C. and O'Hagan, A. (2001). Bayesian calibration of computer models. *Journal of the Royal Statistical Society: Series B*, 63(3):425–464.
- Kohler, L., Heifetz, A., Weathered, M., and Cilliers, A. (2023). LSTM Autoencoder Prediction of Distributed Temperature in Liquid Sodium using Measurements with Co-located Fiber Optic Sensor and Sparse Multi-Point Thermocouple Array. In *Transactions of the American Nuclear Society*, Washington, D.C., USA. November 12–15, 2023.
- Kohler, L., Lisowski, D., and Heifetz, A. (2024a). Global Sensitivity Analysis of Distributed Fiber Optic Temperature Measurements in a Thermal Hydraulic System. In *Transactions of the 2024 International Congress on Advances in Nuclear Power Plants*, Las Vegas, Nevada, USA. June 16–19, 2024.
- Kohler, L., Weathered, M., and Heifetz, A. (2024b). Compression Multimodal Learning for Reconstruction of Temperature Field from Sparse Measurements in a Liquid Metal Cooled Reactor. (In preparation, to be submitted to *Scientific Reports*).
- Kohler, L., Weathered, M., and Heifetz, A. (2024c). VOCAL: Validation, Optical Calibration and Learning Interactive Graphical Interface for Distributed Temperature Sensing in Advanced Reactors. In *Transactions of Advances in Thermal Hydraulic Conference*, Orlando, Florida, USA. November 17–21, 2024.
- Kohler, L., Weathered, M., Lisowski, D., Wu, X., and Heifetz, A. (2024d). Bayesian calibration and sensitivity analysis of fiber optic distributed temperature sensing in water. *Nuclear Science and Engineering*. Submitted.
- Kohler, L., Wu, X., and Heifetz, A. (2024e). Bayesian Inference and Inverse Uncertainty Quantification of Fiber Optic Distributed Temperature Sensing in a Thermal Mixing Tee. In *Proceedings of the ANS Best Estimate Plus Uncertainty International Conference (BEPU-2024)*, Lucca, Tuscany, Italy. May 19–24, 2024, Submitted.
- Korganbayev, S., De Landro, M., Morra, F., Cigada, A., and Saccomandi, P. (2020). Fiber optic sensors for distributed and quasi-distributed temperature measurement. In *2020 IEEE sensors*, pages 1–4. IEEE.
- Korsah, K., Kisner, R., Britton Jr, C., Ramuhalli, P., Wootan, D., Anheier Jr, N., Diaz, A., Hirt, E., Vilim, R. B., Chien, H., et al. (2016). Assessment of sensor technologies for advanced reactors. Technical report, Oak Ridge National Laboratory (ORNL), Oak Ridge, TN (United States).
- Kovesdi, C. R., Spielman, Z. A., Mohon, J. D., Miyake, T. M., Hill, R. A., and Pederson, C. (2021). Development of an assessment methodology that enables the nuclear industry to evaluate adoption of advanced automation. Technical report, Idaho National Lab.(INL), Idaho Falls, ID (United States).
- Kumar, V. D., Bhattacharyya, A., Behera, R. P., Kasinathan, M., and Prabakar, K. (2025). Degradation and residual life assessment of thermocouples with damaged sheaths in corrosive environments. *Journal of Instrumentation*, 20(01):P01002.

- Lange, S. and Riedmiller, M. (2010). Deep auto-encoder neural networks in reinforcement learning. In *The 2010 international joint conference on neural networks (IJCNN)*, pages 1–8. IEEE.
- Langer, J., Jimenez de Aberasturi, D., Aizpurua, J., Alvarez-Puebla, R. A., Auguie, B., Baumberg, J. J., Bazan, G. C., Bell, S. E., Boisen, A., Brolo, A. G., et al. (2019). Present and future of surface-enhanced raman scattering. *ACS nano*, 14(1):28–117.
- Lenner, M., Frank, A., Yang, L., Roininen, T. M., and Bohnert, K. (2019). Long-term reliability of fiber-optic current sensors. *IEEE Sensors Journal*, 20(2):823–832.
- Lu, P., Lalam, N., Badar, M., Liu, B., Chorpening, B. T., Buric, M. P., and Ohodnicki, P. R. (2019). Distributed optical fiber sensing: Review and perspective. *Applied Physics Reviews*, 6(4).
- Marques, J. (2011). Review of generation-III/III+ fission reactors. *Nuclear energy encyclopedia: Science, technology, and applications*, pages 231–254.
- Medsker, L. R., Jain, L., et al. (2001). Recurrent neural networks. *Design and Applications*, 5(64-67):2.
- Mignacca, B., Locatelli, G., and Sainati, T. (2020). Deeds not words: Barriers and remedies for small modular nuclear reactors. *Energy*, 206:118137.
- Morris, M. D. (1991). Factorial sampling plans for preliminary computational experiments. *Technometrics*, 33(2):161–174.
- Nayak, A. and Sinha, R. (2007). Role of passive systems in advanced reactors. *Progress in Nuclear Energy*, 49(6):486–498.
- Noh, S.-H. (2021). Analysis of gradient vanishing of rnns and performance comparison. *Information*, 12(11):442.
- O’Hagan, A. (2006). Bayesian analysis of computer code outputs: a tutorial. *Reliability Engineering & System Safety*, 91(10):1290–1300.
- Omar, H., Graetz, G., and Ho, M. (2022). Decarbonizing with nuclear power, current builds, and future trends. *The 4Ds of Energy Transition: Decarbonization, Decentralization, Decreasing Use and Digitalization*, pages 103–151.
- Palmer, A., Haggard, D., Herter, J., Scervini, M., Swank, W., Knudson, D., and Cherry, R. (2015). Summary of thermocouple performance during advanced gas reactor fuel irradiation experiments in the advanced test reactor and out-of-pile thermocouple testing in support of such experiments. In *2015 4th International Conference on Advancements in Nuclear Instrumentation Measurement Methods and their Applications (ANIMMA)*, pages 1–9. IEEE.
- Pantopoulou, S., Ankel, V., Weathered, M. T., Lisowski, D. D., Cilliers, A., Tsoukalas, L. H., and Heifetz, A. (2022). Monitoring of temperature measurements for different flow regimes in water and galinstan with long short-term memory networks and transfer learning of sensors. *Computation*, 10(7):108.

- Reales Gutiérrez, G., van Keulen, A., Goosen, J., Aragón, A. M., and Bornheim, A. (2024). Enhancing the cooling performance of thermocouples.
- Rempe, J. L., Knudson, D. L., Condie, K. G., Crepeau, J. C., Daw, J. E., and Wilkins, S. C. (2009). Options extending the applicability of high-temperature irradiation-resistant thermocouples. *Nuclear technology*, 167(1):169–177.
- Rovera, A., Tancau, A., Boetti, N., Dalla Vedova, M. D., Maggiore, P., and Janner, D. (2023). Fiber optic sensors for harsh and high radiation environments in aerospace applications. *Sensors*, 23(5):2512.
- Saltelli, A., Ratto, M., Andres, T., Campolongo, F., Cariboni, J., Gatelli, D., Saisana, M., and Tarantola, S. (2008). *Global sensitivity analysis: the primer*. John Wiley & Sons.
- Serp, J., Allibert, M., Beneš, O., Delpech, S., Feynberg, O., Ghetta, V., Heuer, D., Holcomb, D., Ignatiev, V., Kloosterman, J. L., et al. (2014). The molten salt reactor (msr) in generation iv: overview and perspectives. *Progress in Nuclear Energy*, 77:308–319.
- Sharma, S., Sharma, S., and Athaiya, A. (2017). Activation functions in neural networks. *Towards Data Sci*, 6(12):310–316.
- Sobol', I. M. (1990). On sensitivity estimation for nonlinear mathematical models. *Matematicheskoe Modelirovanie*, 2(1):112–118.
- Sobol, I. M. (2001). Global sensitivity indices for nonlinear mathematical models and their monte carlo estimates. *Mathematics and computers in simulation*, 55(1):271–280.
- Stewart, W. R. and Shirvan, K. (2022). Capital cost estimation for advanced nuclear power plants. *Renewable and Sustainable Energy Reviews*, 155:111880.
- Stuart, A. M. (2010). Inverse problems: a bayesian perspective. *Acta numerica*, 19:451–559.
- Tarantola, A. (2005). *Inverse problem theory and methods for model parameter estimation*. SIAM.
- Tierney, L. (1994). Markov chains for exploring posterior distributions. *the Annals of Statistics*, pages 1701–1728.
- Udd, E. and Spillman Jr, W. B. (2024). *Fiber optic sensors: an introduction for engineers and scientists*. John Wiley & Sons.
- Wainwright, H. M., Finsterle, S., Jung, Y., Zhou, Q., and Birkholzer, J. T. (2014). Making sense of global sensitivity analyses. *Computers & Geosciences*, 65:84–94.
- Wang, W., Huang, Y., Wang, Y., and Wang, L. (2014). Generalized autoencoder: A neural network framework for dimensionality reduction. In *Proceedings of the IEEE conference on computer vision and pattern recognition workshops*, pages 490–497.
- Weathered, M. et al. (2019). Thermal hydraulic experimental test article - status report for fy2019 rev. 1. Technical Report ANL-ART-176 Rev. 1, Argonne National Laboratory.

- Weathered, M., Rein, J., Anderson, M., Brooks, P., and Coddington, B. (2017). Characterization of thermal striping in liquid sodium with optical fiber sensors. *Journal of Nuclear Engineering and Radiation Science*, 3(4):041003.
- Wolff, C., Smith, M., Stiller, B., and Poulton, C. (2021). Brillouin scattering—theory and experiment: tutorial. *JOSA B*, 38(4):1243–1269.
- Wu, J. (2018). A basic guide to thermocouple measurements. *Texas Instruments application report*.
- Wu, J., Wang, M., Zhao, K., Huang, S., Zaghoul, M. A., Cao, R., Carpenter, D., Zheng, G., Rountree, S. D., and Chen, K. P. (2021a). Distributed fiber sensors with high spatial resolution in extreme radiation environments in nuclear reactor cores. *Journal of Lightwave Technology*, 39(14):4873–4883.
- Wu, T., Liu, G., Fu, S., and Xing, F. (2020). Recent progress of fiber-optic sensors for the structural health monitoring of civil infrastructure. *Sensors*, 20(16):4517.
- Wu, X. (2017). *Metamodel-based Inverse Uncertainty Quantification of Nuclear Reactor Simulators under the Bayesian Framework*. PhD thesis, University of Illinois at Urbana-Champaign.
- Wu, X., Kozlowski, T., Meidani, H., and Shirvan, K. (2018a). Inverse uncertainty quantification using the modular bayesian approach based on gaussian process, part 1: theory. *Nuclear Engineering and Design*, 335:339–355.
- Wu, X., Kozlowski, T., Meidani, H., and Shirvan, K. (2018b). Inverse uncertainty quantification using the modular bayesian approach based on gaussian process, part 2: Application to trace. *Nuclear Engineering and Design*, 335:417–431.
- Wu, X., Xie, Z., Alsafadi, F., and Kozlowski, T. (2021b). A comprehensive survey of inverse uncertainty quantification of physical model parameters in nuclear system thermal–hydraulics codes. *Nuclear Engineering and Design*, 384:111460.
- Yegnanarayana, B. (2009). *Artificial neural networks*. PHI Learning Pvt. Ltd.
- Young, A. T. (1981). Rayleigh scattering. *Applied optics*, 20(4):533–535.
- Yvon, P. and Carré, F. (2009). Structural materials challenges for advanced reactor systems. *Journal of nuclear materials*, 385(2):217–222.
- Zinkle, S., Terrani, K., and Snead, L. (2016). Motivation for utilizing new high-performance advanced materials in nuclear energy systems. *Current Opinion in Solid State and Materials Science*, 20(6):401–410.
- Zohuri, B. (2020). Generation iv nuclear reactors. In *Nuclear Reactor Technology Development and Utilization*, pages 213–246. Elsevier.

APPENDICES

APPENDIX

A

LIST OF ACRONYMS

A summary of all acronyms is documented in Table A.1.

Table A.1: A summary of acronyms used in alphabetical order.

Acronym	Abbreviation
Autocorrelation Function	ACF
Artificial Neural Network	ANN
Boiling Water Reactor	BWR
Computational Fluid Dynamics	CFD
Convolutional Neural Network	CNN
Distributed Fiber Optic Sensors	DFOS
Delayed Rejection Adaptive Metropolis	DRAM
Distributed Temperature Sensing	DTS
Electrical Engineering	EE
Gallons Per Minute	GPM
Global Sensitivity Analysis	GSA
Intermediate Heat Exchanger	IHX
Inverse Uncertainty Quantification	IUQ
Local Sensitivity Analysis	LSA

Long Short-Term Memory	LSTM
Markov Chain Monte Carlo	MCMC
Mechanisms Engineering Test Loop	METL
Molten Salt Cooled Reactor	MSCR
Operations and Maintenance	O&M
Principal Component Correlation	PCC
Pressurized Water Reactor	PWR
Rectified Linear Unit	ReLU
Recurrent Neural Network	RNN
Sensitivity Analysis	SA
Sodium Fast Reactor	SFR
Spearman Rank Correlation Coefficient	SRCC
Temperature Coefficient	TC
Thermal Hydraulic Experimental Test Article	THETA
Uncertainty Quantification	UQ
Variational Autoencoder	VAE

APPENDIX

B

LIST OF SYMBOLS AND VARIABLES

A summary of all variables is documented in Table B.1.

Table B.1: A summary of common meteorological variables and their abbreviations in alphabetical order.

Variable	Abbreviation
Bayesian inference normalization factor	Z
Calibration coefficient related to frequency shift scaling	$a(\theta_1)$
Covariance matrix of posterior distribution	Σ
Estimated temperature from DFOS calibration equation	T
Exponent term defining the nonlinear response	$b(\theta_2)$
Input feature set for machine learning model	X
Long Short-Term Memory neural network model	$LSTM$
Markov Chain Monte Carlo (MCMC) sample count	N
Measured frequency shift from Rayleigh scattering DFOS	S
Mean of posterior distribution for calibration parameters	μ
Number of training dataset samples for machine learning model	\mathcal{D}
Offset term for temperature correction	$c(\theta_3)$
Pearson Correlation Coefficient (linear dependence)	PCC

Predicted output from machine learning model	Y
Probability density function for Bayesian inference	p
Root Mean Square Error (RMSE) used as evaluation metric	$RMSE$
Sensitivity analysis via variance decomposition (Sobol')	$Sobol'$
Spearman Rank Correlation Coefficient (monotonic dependence)	$SRCC$
Standard deviation of measurement noise	σ
Surrogate model function for temperature prediction	$f(X, \theta)$
Time index for sequential data in LSTM network	t
Weight vector for neural network parameters	ω